iScience

CellPress

Article

Single Atomic Cu-N_2 Catalytic Sites for Highly Active and Selective Hydroxylation of Benzene to Phenol

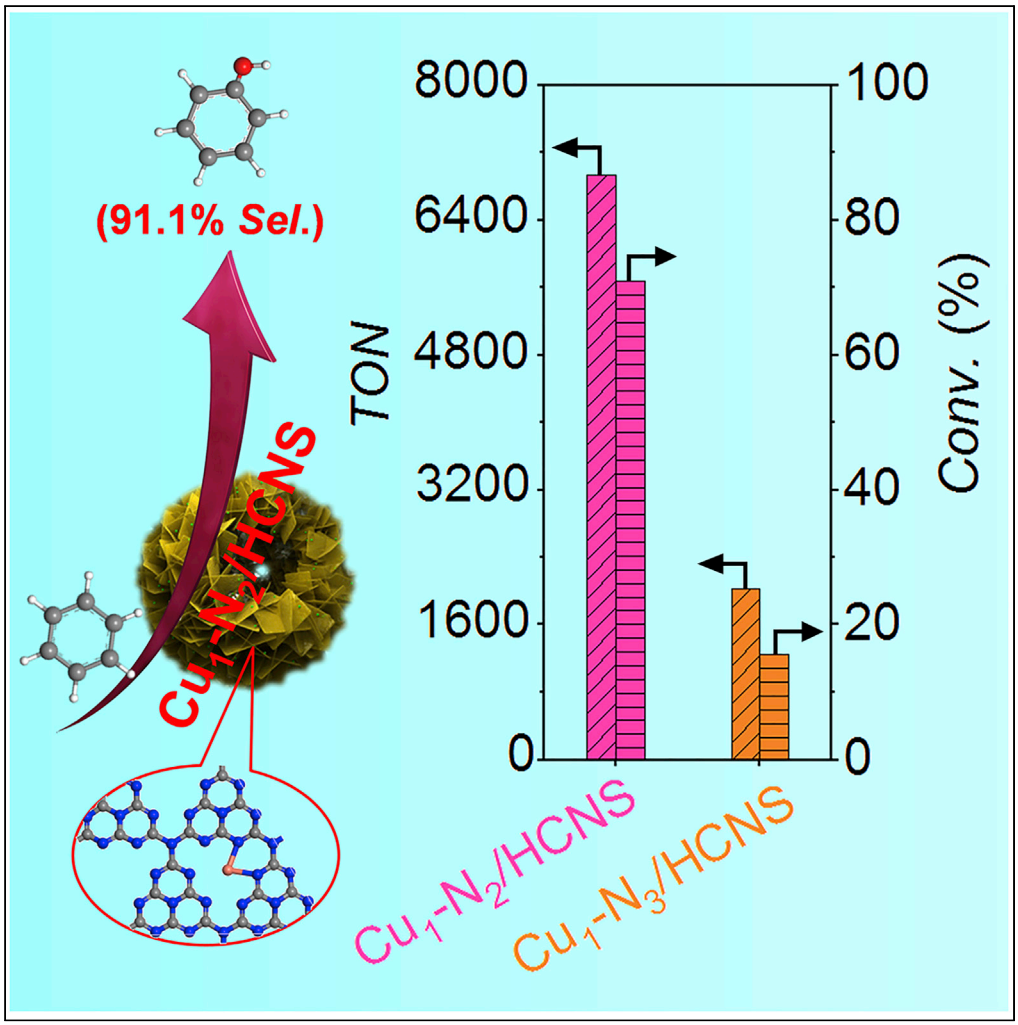

Ting Zhang, Xiaowa Nie, Weiwei Yu, ..., Rui Si, Yuefeng Liu, Zhongkui Zhao

sirui@sinap.ac.cn (R.S.)
yuefeng.liu@dicp.ac.cn (Y.L.)
zkzhao@dlut.edu.cn (Z.Z.)

HIGHLIGHTS

Single-atom Cu catalyst on HCNS with unique Cu-N_2 moieties was synthesized

Cu-N_2 shows 3.4 times turnover number of Cu-N_3 for benzene hydroxylation

Unique Cu-N_2 coordination state leads to lower energy barrier for H_2O_2 activation

It paves a new avenue to design single-atom catalysts by tuning coordination state

Zhang et al., iScience *22*, 97–108
December 20, 2019
https://doi.org/10.1016/j.isci.2019.11.010

iScience

CellPress

Article

Single Atomic Cu-N_2 Catalytic Sites for Highly Active and Selective Hydroxylation of Benzene to Phenol

Ting Zhang,[1,5] Xiaowa Nie,[1,5] Weiwei Yu,[1] Xinwen Guo,[1] Chunshan Song,[1,2] Rui Si,[3,*] Yuefeng Liu,[4,*] and Zhongkui Zhao[1,6,*]

SUMMARY

Searching for an efficient single-atom catalyst for benzene hydroxylation to phenol is of critical importance, but it still remains a challenge. Herein, a single-atom catalyst with unique Cu-N_2 moieties (Cu_1-N_2/HCNS) was prepared and confirmed by HAADF-STEM and EXAFS. Turnover number (TON) over Cu_1-N_2/HCNS (6,935) is 3.4 times of Cu_1-N_3/HCNS (2,034) under the same reaction conditions, and both exhibit much higher phenol selectivity (close to 99%) and stability compared with Cu nanoparticles and nanoclusters. Experiments and DFT calculations reveal that atomically dispersed Cu species are active sites for benzene hydroxylation to phenol, and the Cu-N_2 is more active than Cu-N_3 owing to its much lower energy barrier concerning the activation of H_2O_2 led by its unique coordination state of local atomic structure. We envision that this work opens a new window for modulating coordination environments of single metallic atoms in catalysis design.

INTRODUCTION

Activation of aromatic C-H bonds has been one of the most active research topics, yet long-standing challenge remains (Leitch and Frost, 2017; Sambiagio et al., 2018; Shan et al., 2018). Phenol is widely used as a versatile intermediate for phenolic resin, pharmaceuticals, agrochemicals, etc. (Bal et al., 2006; Wang et al., 2012). However, the current technology for phenol production by three-step cumene process generates large amounts of chemical waste and low-value by-product (Tsuji et al., 2017; Morimoto et al., 2015; Chen et al., 2009). Catalytic direct selective oxidation of benzene with H_2O_2 as oxidant is an acceptable passway for efficient and clean phenol production (Ivanchikova et al., 2014; Su et al., 2017; Evtushok et al., 2018; Xia and Tang, 2012; Szécsényi et al., 2018). In this regard, heterogeneous catalytic hydroxylation of benzene with H_2O_2 to phenol is highly desirable Zhang et al., 2017a, 2017b; Deng et al., 2015; Zhu et al., 2018; Yang et al., 2013; ElMetwally et al., 2018; Han et al., 2017). Although numerous efforts of designing such catalytic system have been made and considerable achievements have been obtained, it still remains a challenge (Balducci et al., 2003). Nitrogen-doped carbon materials have been found to be active for hydroxylation of benzene with H_2O_2 under mild condition yet shows low catalytic activity (Yang et al., 2013). Metal-doped carbon nitride shows an improved activity for hydroxylation of benzene with H_2O_2 to phenol but still remains unsatisfactory (Chen et al., 2009; Di et al., 2010; Xu et al., 2018; Zhang et al., 2018a, 2018b; Hosseini et al., 2018). Therefore, developing efficient catalysts for benzene hydroxylation with H_2O_2 to phenol is of great urgency.

Owing to enhanced intrinsic activity and selectivity toward targeted product and maximized utility of metal atoms (Dvořák et al., 2016; Kwon et al., 2017; Chen et al., 2018a, 2018b; Yamaguchi et al., 2017; Li et al., 2018a, 2018b; Malonzo et al., 2016; Liang et al., 2015), single-atom catalyst (SAC) has been emerging as an attractive frontier in heterogeneous catalysis (Qiao et al., 2011; Mitchell et al., 2018; Chen et al., 2018a, 2018b; Thomas et al., 2005; Yamashita et al., 2018). Up to now, SAC has been broadly applied to thermo-, electro-, and photo-catalysis owing to its extraordinary catalytic performance from the unique electronic properties of single atomic sites (Zhang et al., 2018a, 2018b; Gao et al., 2016; bin Mohd Yusoff et al., 2015; Yang et al., 2016; Cheng et al., 2018). Especially for the activation of C-H bonds, SAC shows extraordinary catalysis than nanoparticles (Marcinkowski et al., 2018; Yuan et al., 2018; Yamaguchi et al., 2018). Single-atom Fe/Ni/Co materials are proved to be efficient for benzene hydroxylation with H_2O_2 to phenol (Ivanchikova et al., 2014; Su et al., 2017; Evtushok et al., 2018; Wang et al., 2015). However, the activity and selectivity are far from their applications. Our previous work shows that single atomic Cu-N_3 sites

[1]State Key Laboratory of Fine Chemicals, PSU-DUT Joint Center for Energy Research, School of Chemical Engineering, Dalian University of Technology, Dalian 116024, P. R. China

[2]EMS Energy Institute PSU-DUT Joint Center for Energy Research and Department of Energy & Mineral Engineering and Chemical Engineering, Pennsylvania State University, University Park, PA 16802, USA

[3]Shanghai Synchrotron Radiation Facility, Shanghai Institute of Applied Physics, Chinese Academy of Sciences, Shanghai 201204, P. R. China

[4]Dalian National Laboratory for Clean Energy, Dalian Institute of Chemical Physics, Chinese Academy of Sciences, Dalian 116023, P. R. China

[5]These authors contributed equally.

[6]Lead Contact

*Correspondence: sirui@sinap.ac.cn (R.S.), yuefeng.liu@dicp.ac.cn (Y.L.), zkzhao@dlut.edu.cn (Z.Z.)

https://doi.org/10.1016/j.isci.2019.11.010

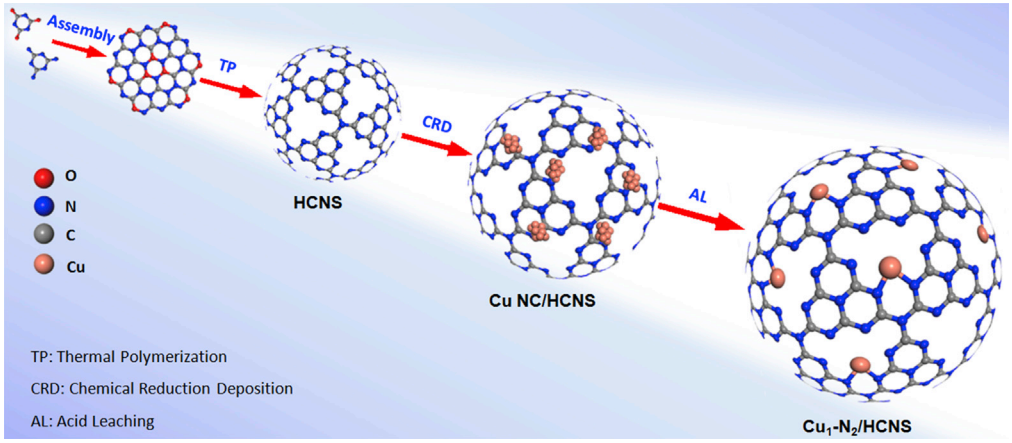

Scheme 1. Schematic Illustration of the Preparation of Single-Atom Cu1-N2/HCNS Catalyst

have extraordinary phenol selectivity with H_2O_2 as oxidant, yet the activity still remains to be improved (Zhang et al., 2018a, 2018b). Therefore, developing single-atomic Cu catalysts with increased activity for benzene hydroxylation with H_2O_2 is desirable. In homogeneous catalysis, the design of ligands plays crucial roles in tuning activity by modulating the coordination states of central metal atoms (Morimoto et al., 2015). Also for heterogeneous catalysis, as reported by references Evtushok et al., 2018; Liu et al., 2017; Jiang et al., 2018; Han et al., 2018, the coordination states of metal atom in SAC significantly affect the catalytic performance. Considering this, modulating coordinated state of single-atom Cu-N_x moieties on hollow carbon nitride microsphere (HCNS) can be a sapiential approach to develop an excellent single-atom catalyst for benzene hydroxylation to phenol.

Herein, a single-atom Cu catalyst isolated on HCNS with unique Cu-N_2 moieties (Cu_1-N_2/HCNS) has been successfully prepared by a facile chemical reduction deposition-acid leaching (CRD-AL) method (see Scheme 1), confirmed by extended X-ray absorption fine structure (EXAFS) and high-angle annular dark-field scanning transmission electron microscopy (HAADF-STEM). Surprisingly, Cu_1-N_2/HCNS exhibits 3.4 times turnover number (*TON*) (6,935) of Cu_1-N_3/HCNS (2,034) toward benzene hydroxylation to phenol; besides, both single-atom catalysts demonstrate much higher selectivity and stability than Cu nanoparticles or nanoclusters. HAADF-STEM, EXAFS, and kinetic results reveal that the single-atom Cu species are catalytic active sites for benzene hydroxylation to phenol and Cu-N_2 is extremely more active than Cu-N_3 owing to its unique local atomic structure.

RESULTS AND DISCUSSION

Synthesis and Characterization of Cu_1-N_2/HCNS Catalyst

In this paper, a single-atom Cu catalyst isolated on HCNS with unique Cu-N_2 moieties (Cu_1-N_2/HCNS) has been successfully prepared by a facile CRD-AL method. Typically, 0.14 g of HCNS carrier (Jun et al., 2013a, 2013b) was first ultrasonically dispersed in 20 mL of $Cu(NO_3)_2$ aqueous solution (2 mmol L^{-1}). Then, the Cu species were deposited on HCNS surface with 1 mL of $NaBH_4$ (0.5 mol L^{-1}) as reductant. After stirring for 4 h at room temperature, solid sample was collected by centrifugation and washed with DI water and ethanol three times, respectively. Subsequently, the solid sample was dried at 60°C for 12 h. For now, the obtained dry solid catalyst is denoted as Cu NC/HCNS (1.14 wt% Cu, inductively coupled plasma-atomic emission spectrometry [ICP-AES]). To get single-atom catalyst Cu_1-N_2/HCNS, 0.01 g of Cu NC/HCNS was further treated with 10 mL of dilute HNO_3 solution for 4 h at room temperature. The solid was centrifuged, washed with DI water to neutral and dried at 60°C for 4 h. The finally acquired solid catalyst was named as Cu_1-N_2/HCNS (0.23 wt% Cu, ICP-AES). During the acid-leaching process, the CuO nanoclusters are easily eliminated, whereas the single atoms anchored by the support are stable (Liu et al., 2018). Although metallic Cu can be oxidized, in our synthetic system with massive excess $NaBH_4$, the Cu^{2+} captured by N atoms on HCNS can be *in situ* reduced and single-atomic Cu coordinated with neighboring N atoms formed. The method applied in this work is different from the pre-assembly method for Cu-N_3 in our former report (Zhang et al., 2018a, 2018b). For Cu_1-N_2/HCNS catalyst, the Cu species were deposited on the pre-formed HCNS, followed by

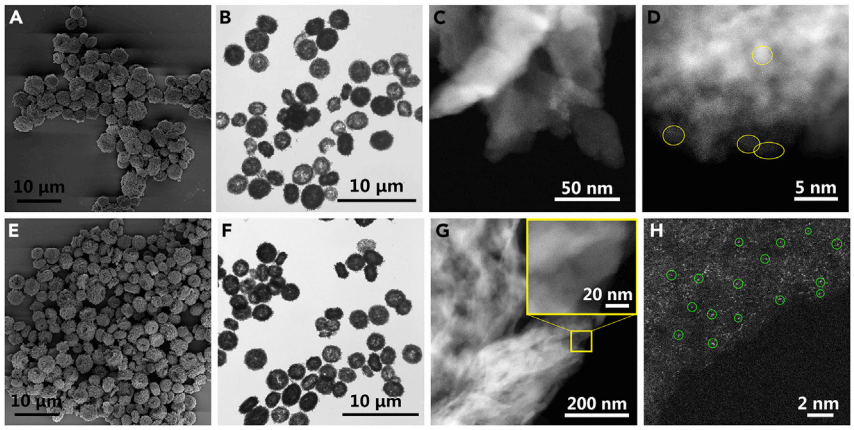

Figure 1. Characterization of As-prepared Samples

(A and B) Scanning electron microscopy (SEM) (A) and transmission electron microscopy (TEM) (B) images of Cu NC/HCNS catalyst.

(C and D) HAADF-STEM images of Cu NC/HCNS catalyst, the Cu clusters are highlighted by yellow circles.

(E and F) SEM (E) and TEM (F) images of Cu_1-N_2/HCNS catalyst.

(G and H) HAADF-STEM images of Cu_1-N_2/HCNS catalyst, the single Cu atoms are highlighted by green circles.

acid-leaching treatment; CuOx clusters were removed while the single-atomic Cu was anchored by two neighboring N atoms and formed the Cu-N_2 sites, whereas for the Cu_1-N_3/HCNS catalyst, the Cu^{2+} ions were pre-coordinated with melamine to form Cu-Mel complex and the Cu atoms were isolated in the supermolecular assemblies; subsequently, Cu-N_3 sites were *in situ* formed during thermal polymerization.

X-ray powder diffraction (XRD) patterns of Cu NC/HCNS and Cu_1-N_2/HCNS catalysts (see Figure S1) display the characteristic peaks at 12.9° and 27.4°, assigned to (100) and (200) crystal faces of g-C_3N_4, respectively (Zhao et al., 2018), indicating deposition and acid leaching have no influence on the crystal property of g-C_3N_4 support. Field emission scanning electron microscopy and transmission electron microscopy (see Figures 1A, 1B, 1E, 1F, and S2A) are applied for characterization toward the morphology of as-prepared catalysts. It is shown that Cu_1-N_2/HCNS and Cu NC/HCNS catalysts feature a regular hollow spherical structure (Zhang et al., 2018a, 2018b; Jun et al., 2013a, 2013b). Textural properties (see Figure S3 and Table S1) indicate that the micro-structure of HCNS is maintained after loading Cu atoms. The porous hollow micro-/nano-structures have benefit for the catalytic reaction by improving accessibility of catalytic sites to reactants (Zhang et al., 2018a, 2018b; Harmer et al., 1996; Matei et al., 2013; Li et al., 2018a, 2018b). Furthermore, the textural properties of CN_1-N_2/HCNS and Cu_1-N_3/HCNS are similar. Also, our former research indicates that the elemental composition of Cu_1-N_3/HCNS is same as the HCNS support (molar ratio of N/C = 1.5) (Zhang et al., 2018a, 2018b). The addition of trace Cu-melamine complex (0.85 wt% Cu in the final Cu_1-N_3/HCNS catalyst) shows inconspicuous effect on the textural properties of Cu_1-N_3/HCNS catalyst compared with the HCNS support.

For further observation of metal species dispersed on g-C_3N_4 support, HAADF-STEM experiments were performed and the obtained images are displayed in Figures 1C, 1D, 1G, and 1H. No obvious metallic nanoparticles can be observed both on Cu NC/HCNS and Cu_1-N_2/HCNS. XRD patterns (see Figure S1) also exhibit no characteristic peak corresponding to Cu nanoparticles. However, HAADF-STEM image (see Figure 1D) of Cu NC/HCNS displays the existence of nanoclusters less than 2 nm. The fitting results (see Table S2) toward R-space EXAFS spectrum (see Figure S4) of Cu NC/HCNS are matched well with CuO_x clusters, i.e., first shell of Cu-O at 1.92 Å with CN = 2.9 and second shell of Cu-Cu (originated from Cu-O-Cu) at 2.87 Å with 0.4 of coordination (CN). Besides, X-ray photoelectron spectroscopy (XPS) of O 1s spectrum (see Figure S5A) reveals the existence of lattice O^{2-} species and the N 1s XPS spectrum (see Figure S5B) displays no obvious peak assigned to Cu-N species, further proving the CuO_x clusters on the Cu NC/HCNS. For clear observation, the raw and enlarged image of Figure 1D is given in Figure S2B. Concerning Cu_1-N_2/HCNS catalyst, single Cu atoms are clearly identified as bright spots (highlighted by green circles) isolated on g-C_3N_4 surface by HAADF-STEM image (see Figure 1I). The Cu content of Cu_1-N_2/HCNS is ca. 0.23 wt% determined by inductively coupled plasma-atomic emission spectroscopy.

The amount of active Cu sites in single-atom Cu_1-N_2/HCNS catalyst is determined by KSCN titration method, and the results are shown in Figure S6. The result indicates that, for Cu_1-N_2/HCNS catalyst, about 80% of the loaded Cu atoms serve as active sites (0.029 $mmol_{Cu}/g_{Cat.}$) (see Figure S6A), whereas for Cu_1-N_3/HCNS, about 60% of the loaded Cu atoms serve as active sites (0.080 $mmol_{Cu}/g_{Cat.}$) (see Figure S6B).

Heteroatom, like N atoms, in carbon matrix have been proved to be efficient anchoring sites for stabilizing metal atoms (Zhang et al., 2018a, 2018b; Liu et al., 2018; Qu et al., 2018). g-C_3N_4 features abundant N content and chemical stability (Liu et al., 2016) and, therefore, has been considered as an ideal support for single-atom catalysts (Zhang et al., 2018a, 2018b). For understanding the electronic character of the developed Cu_1-N_2/HCNS catalyst, X-ray photoelectron spectroscopy (XPS) was carried out (see Figures 2 and S7). XPS survey spectrum of Cu_1-N_2/HCNS (see Figure S7A) displays the characteristic peaks of C, N, O, and Cu. The deconvoluted O 1s spectrum (see Figure 2A) shows no lattice O^{2-} species, proving the complete etching of Cu_xO clusters. C 1s spectrum (see Figure S7B) reveals the major content of C-C, N-C=N species, whereas the deconvoluted N 1s spectrum of Cu_1-N_2/HCNS (see Figure 2B) features an extra peak (399.0 eV) assigned to Cu-N species (Zhang et al., 2017a, 2017b), besides the characteristic peaks belonging to pyridinic-N (398.5 eV), pyrrolic-N (400.1 eV), and graphitic-N (401.0 eV) compared with HCNS matrix. The strong coordination of Cu atom with surrounding N atoms in the g-C_3N_4 matrix stabilizes the atomically dispersed Cu sites. Cu 2p XPS spectra (see Figure 2C) show that the characteristic peak of Cu^+ $2p_{3/2}$ shifts to 932.8 eV in single-atom Cu_1-N_2/HCNS compared with that of Cu NC/HCNS, further confirming the strong interaction between single Cu atoms and the g-C_3N_4 matrix.

To further investigate the electronic properties and coordination environment of Cu_1-N_2/HCNS, X-ray absorption near-edge spectroscopy (XANES) and EXAFS measurements were performed. Cu *K*-edge XANES profiles for the measured sample and the related references (Cu foil, Cu_2O, and CuO) are shown in Figure 2D. Cu_1-N_2/HCNS exhibits an energy absorption edge between Cu^+ (Cu_2O) and Cu^{2+} (CuO) standards in the range of E_0 (around 8,979 eV), and the corresponding oxidation state of copper is determined as +1.5 via linear combination fitting (Frenkel et al., 2011). This observation agrees with the related XPS results (see Figure 2C). EXAFS spectra (see Figure 2E) for Cu_1-N_2/HCNS only displays a prominent peak at approximately 1.9 Å, and no significant contribution for metallic Cu or oxidized CuO_x clusters at longer distances above 2.5 Å is observed, revealing the atomic dispersion of isolated Cu atoms throughout HCNS matrix. XANES is the nowadays the most direct and efficient technology for the characterization concerning atomic structure of single-atom catalyst. The XANES spectra of central atoms with different coordination numbers or ligands usually display distinct difference in adsorption curves (Kau et al., 1987; Sorrell and Malachowski, 1983; Sorrell et al., 1982). The near-edge of Cu_1-N_2/HCNS and Cu_1-N_3/HCNS (see Figure 2F) features obviously different shapes, implying the possible difference in coordination environment of single-atom Cu moieties. The Cu *K*-edge spectrum of Cu_1-N_2/HCNS is similar to that of the compound Cu(pze)BF_4, in which the central Cu ion is coordinated with N_2O-ligation (Kau et al., 1987; Sorrell and Malachowski, 1983). However, Cu_1-N_3/HCNS catalyst shows a similar Cu *K*-edge spectrum to compound $[Cu_2(mxyN_6)](BF_4)_2$, in which the central Cu ion is coordinated with N_3-ligation (Kau et al., 1987; Sorrell et al., 1982). This difference in the adsorption curve of XANES spectra indicates that the local atomic structure of single Cu atoms over Cu_1-N_2/HCNS differs from that over Cu_1-N_3/HCNS. To further obtain the structural parameters of copper in Cu_1-N_2/HCNS, we conducted EXAFS fitting in R space (see Figure 2G) via a possible structural model presented in Figure 2I. Two nitrogen atoms are coordinated with isolated copper center, which is also capped by adsorbed oxygen-containing molecule (O_2 and/or H_2O and/or CO_2) to form saturated structure for its stable existence. Table S3 shows that the bond length of Cu-N is determined to be 1.92 Å, plus a minor Cu-O shell at 1.96 Å with the coordination number of ca. 1. All these results are well consistent with the hypothesized structural model (see Figure 2I) in the density functional theory (DFT) calculation. For comparison of the reaction mechanism of H_2O_2 activation over Cu_1-N_2/HCNS and Cu_1-N_3/HCNS, the structure model of Cu-N_3 has been constructed and optimized via DFT according to the EXAS fitting results (see Figures 2F, S4D, and S4E and Table S2) and displayed in Figures 2H and 2J.

Catalytic Evaluation

As a critically important chemical transformation, aromatic C-H bond activation has been one of the most active research topics (Morimoto et al., 2015; Marcinkowski et al., 2018; Shilov and Shul'pin, 1997; Labinger and Bercaw, 2002; Wencel-Delord; Glorius, 2013). Herein, benzene hydroxylation with H_2O_2 to phenol was performed as a model reaction to evaluate the catalytic performance of the developed Cu_1-N_2/HCNS catalyst (see Figure 3 and Table S4). For comparison, Cu NC/HCNS, Cu NP/HCNS, and our previously reported

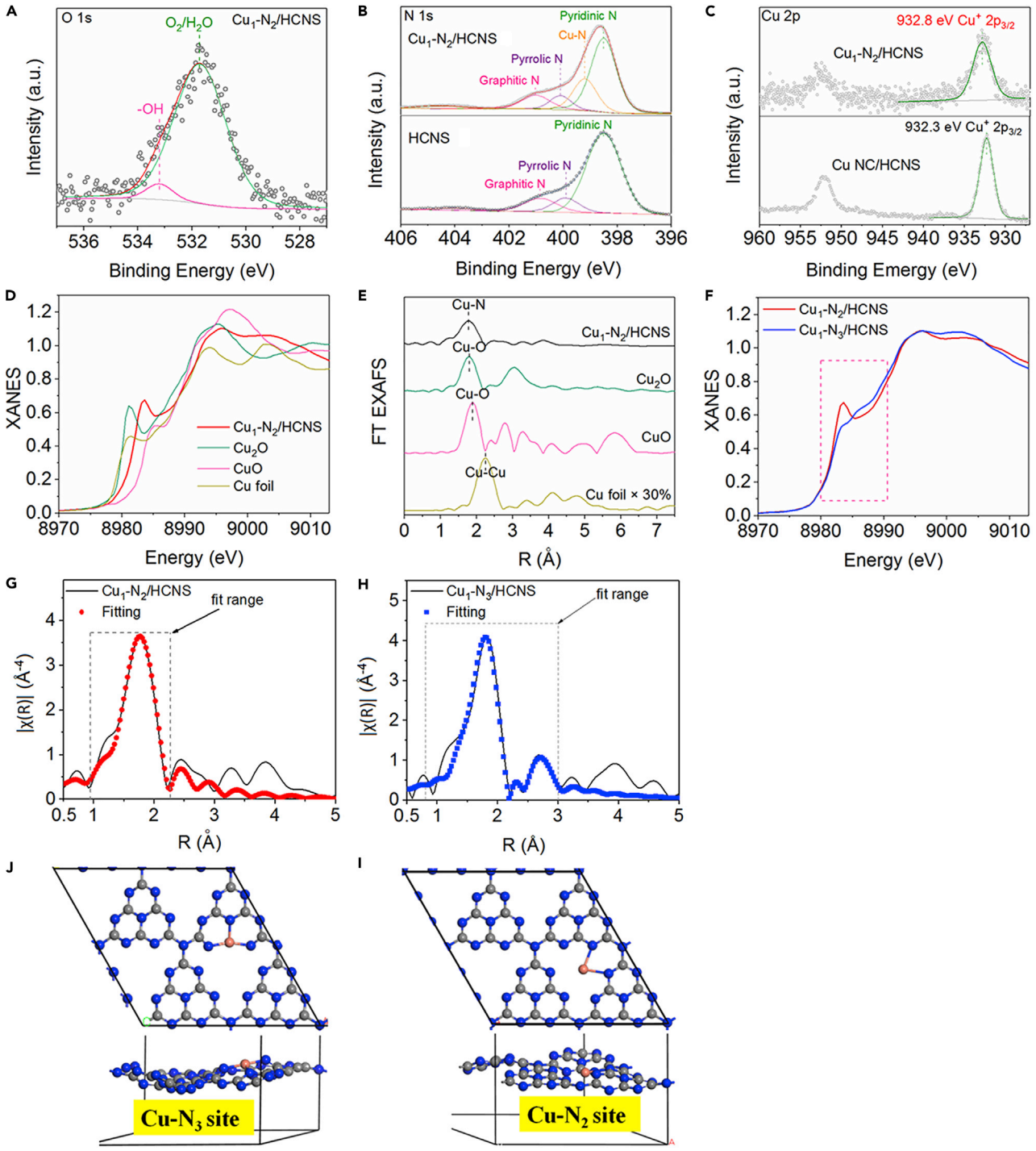

Figure 2. X-Ray Spectroscopy Analyses of single-atom catalyst

(A) The O 1s XPS spectrum of Cu_1-N_2/HCNS single-atom catalyst.

(B) The N 1s XPS spectra of single-atom Cu_1-N_2/HCNS catalyst and HCNS support.

(C) Cu 2p XPS spectra of Cu_1-N_2/HCNS single-atom catalyst and Cu NC/HCNS nanocluster catalyst.

(D and E) Normalized Cu *K*-edge XANES spectra (D) and k^3-weighted Fourier transform spectra (E) from Cu *K*-edge EXAFS of Cu foil, CuO, Cu_2O, and Cu_1-N_2/HCNS.

(F) The comparison of normalized Cu *K*-edge XANES spectra of Cu_1-N_2/HCNS and Cu_1-N_3/HCNS (Zhang et al., 2018a, 2018b).

(G and H) The corresponding EXAFS fitting curves of Cu_1-N_2/HCNS (G) and Cu_1-N_3/HCNS (H).

(I and J) The models of Cu−N_2 sites in Cu_1-N_2/HCNS (I) and the model of Cu−N_3 sites in Cu_1-N_3/HCNS (J), orange, Cu; gray, C; blue, N; red, O.

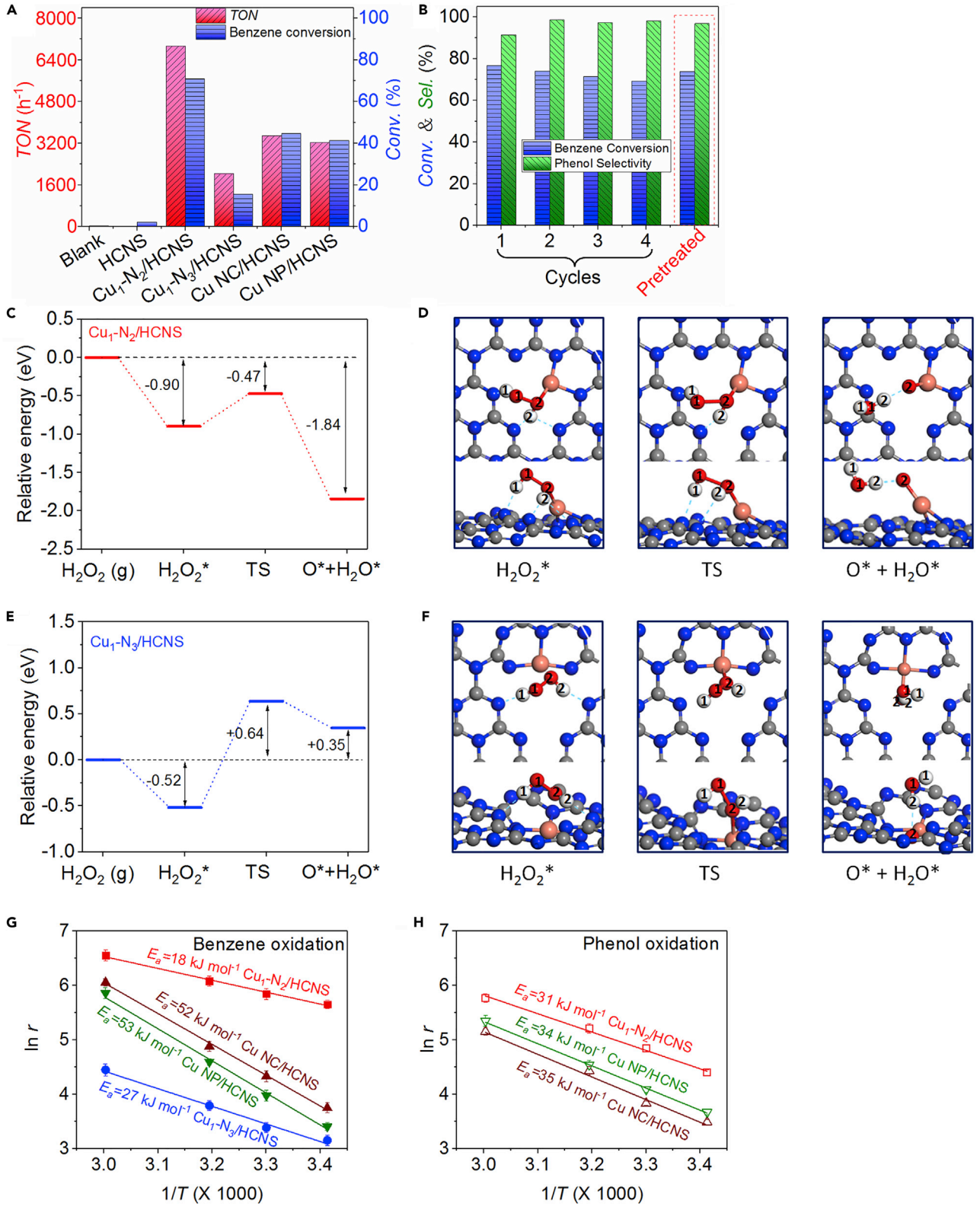
A
TON
Benzene conversion
TON (h-1)
Conv. (%)
Blank
HCNS
Cu1-N2/HCNS
Cu1-N3/HCNS
Cu NC/HCNS
Cu NP/HCNS
B
Conv. & Sel. (%)
Benzene Conversion
Phenol Selectivity
Cycles
Pretreated
C
Cu1-N2/HCNS
Relative energy (eV)
-0.90
-0.47
-1.84
H2O2 (g)
H2O2*
TS
O*+H2O*
D
H2O2*
TS
O* + H2O*
E
Cu1-N3/HCNS
Relative energy (eV)
+0.64
+0.35
-0.52
H2O2 (g)
H2O2*
TS
O*+H2O*
F
H2O2*
TS
O* + H2O*
G
Benzene oxidation
Ea=18 kJ mol-1 Cu1-N2/HCNS
Ea=52 kJ mol-1 Cu NC/HCNS
Ea=53 kJ mol-1 Cu NP/HCNS
Ea=27 kJ mol-1 Cu1-N3/HCNS
ln r
1/T (X 1000)
H
Phenol oxidation
Ea=31 kJ mol-1 Cu1-N2/HCNS
Ea=34 kJ mol-1 Cu NP/HCNS
Ea=35 kJ mol-1 Cu NC/HCNS
ln r
1/T (X 1000)

Figure 3. Catalytic Evaluation Results

(A) Catalytic activity for benzene hydroxylation to phenol over various catalysts. Reaction conditions: 0.013 mol% active copper, molar ratio of H_2O_2 to substrate is 10:1, 0.5 mL of benzene, 6 mL of CH_3CN, 60°C, 12 h for blank/HCNS, 2.5 h for the others.

(B) Recyclability of single-atom Cu_1-N_2/HCNS catalyst. Reaction conditions: 0.013 mol% active copper, molar ratio of H_2O_2 to substrate is 10:1, 0.5 mL of benzene, 6 mL of CH_3CN, 2.5 h.

(C–F) Reaction pathways and energy diagrams for H_2O_2 activation and dissociation over Cu_1-N_2/HCNS (C and D) and Cu_1-N_3/HCNS catalysts (E and F). The values denote the relative energies referenced to the H_2O_2 molecule in gas phase together with the bare catalyst (gray, C; blue, N; orange, Cu; red, O; white, H).

(G and H) Arrhenius plot of diverse catalysts for benzene oxidation (G) and phenol oxidation (H), respectively. The "*r*" for c,d is reaction rate. Reaction conditions: 20 mg of catalyst, 0.20 mL of benzene/phenol, 3.0 mL of H_2O_2 (30 wt%), 6 mL of CH_3CN, 1.5 h.

Cu_1-N_3/HCNS (Zhang et al., 2018a, 2018b) were chosen as benchmark under the same reaction conditions. The results show that only trace benzene is converted without catalyst (Blank) or over bare HCNS support. Like our previously reported Cu_1-N_3/HCNS (Zhang et al., 2018a, 2018b), the developed single atomic Cu_1-N_2/HCNS catalyst exhibits much higher selectivity and stability than Cu nanoparticles and nanoclusters for benzene hydroxylation to phenol. More interestingly, Cu_1-N_2/HCNS catalyst exhibits 3.4 times *TON* (6,935) of Cu_1-N_3/HCNS (2,034) under the same reaction conditions. From Table S4, under the same reaction conditions, 70.9% of benzene conversion with 91.3% of phenol selectivity over Cu_1-N_2/HCNS catalyst can be achieved, whereas only 15.6% of conversion over Cu_1-N_3/HCNS can be obtained, although it shows 99.3% of slightly higher selectivity. In fact, the more than 99.9% of selectivity is also obtained in the absence of catalyst or over the bare HCNS support. Furthermore, the developed Cu_1-N_2/HCNS catalyst also shows much superior catalytic performance to the previously reported single-atom catalysts (Table S4), owing to the atomically dispersed Cu-N_2 moieties and the promoted accessibility of single Cu active sites by the porous hollow structure. Beyond the remarkable catalytic performance, the Cu_1-N_2/HCNS catalyst also shows high recycling stability and reusability. Figure 3B displays no obvious decrease in benzene conversion over Cu_1-N_2/HCNS after four cycles.

It has been revealed that the reaction parameters, such as molar ratio of H_2O_2 to benzene, reaction temperature, and type of catalyst, may affect the performance of liquid phase benzene oxidation over heterogeneous catalysts with H_2O_2 as oxidant (Evtushok et al., 2018; Acharyya et al., 2014). Data in Table S4 (Entry 3 and 12) demonstrate that the reaction temperature has an effect on the catalytic activity and selectivity of benzene oxidation over Cu_1-N_2/HCNS. When the reaction is carried out at 25°C, higher benzene *TON* compared with references is obtained, yet the phenol selectivity shows a disadvantage (see Table S4, Entry 12, 13, and 14). Surprisingly, when the reaction is carried out at 60°C (see Table S4, Entry 3), improved phenol selectivity with enhanced catalytic activity is obtained. The above-mentioned results indicate that a higher reaction temperature (60°C) may be beneficial for the improving of phenol selectivity over Cu_1-N_2/HCNS. This phenomenon is different from the reported results that high temperature leads to decreased phenol selectivity over single-atom Co-ISA/CNS catalyst (Evtushok et al., 2018).

Figure S8 gives the effect of molar ratio of H_2O_2 to benzene in liquid phase benzene oxidation over the Cu_1-N_2/HCNS catalyst. The results clearly show that increasing the molar ratio of H_2O_2 to benzene (less than 10) leads to higher benzene conversion with invariable H_2O_2 utilization and phenol selectivity. However, when the molar ratio of H_2O_2 to benzene is further increased to 15, the benzene conversion displays no more observable increment, yet the H_2O_2 shows striking decrease.

From the aforementioned description, both the Cu_1-N_2/HCNS developed in this work and the Cu_1-N_3/HCNS reported in our previous work feature the single-atom catalyst, however, with different local atomic structures of Cu atoms. Different coordination environment of single-atom Cu catalyst results in quite distinct catalytic performance for liquid phase benzene oxidation (see Table S4, Entry 3 and 4). As previously reported (Ivanchikova et al., 2014; Su et al., 2017; Evtushok et al., 2018), the reaction pathway for benzene oxidation to phenol by H_2O_2 usually can be abstracted into two steps, including the first H_2O_2 decomposition for the formation of active oxygen species and the subsequent oxidation of benzene to phenol. The much different catalytic activity clearly displays that the benzene conversion is directly related to the H_2O_2 conversion since a similar H_2O_2 utilization efficiency over Cu_1-N_2/HCNS, Cu_1-N_3/HCNS, and Cu NC/HCNS catalysts can be observed (see Table S4, Entry 3, 4, and 5). This phenomenon implies that the different catalytic performance over diverse catalysts may derive from their discrepant abilities for the activation of H_2O_2.

DFT Calculations for Reaction Mechanism

To compare the activity of Cu_1-N_2/HCNS and Cu_1-N_3/HCNS catalysts toward H_2O_2 adsorption and activation, DFT calculations were performed to identify intermediates and reaction pathways. The minimum energy pathways for H_2O_2 adsorption and dissociation on the Cu-N_2 and Cu-N_3 sites are illustrated in Figures 3C–3F, respectively, with all optimized structures included. On the Cu_1-N_2/HCNS catalyst, the H_2O_2 oxidant is initially adsorbed by the active Cu site with the O-Cu_2 distance of 1.90 Å. In the meantime, multiple hydrogen bonds are formed between the H atoms of H_2O_2 and N atoms of the catalyst, resulting in an activation of the O-O bond to1.51 Å from 1.48 Å in gas phase. The binding energy of H_2O_2 is calculated to be −0.89 eV on the Cu-N_2 site. The activated H_2O_2* can be easily transformed into the active O* species by releasing a water molecule, with an energy barrier of only 0.42 eV and a reaction energy exothermic by −0.95 eV. As shown in the transition state configuration (see Figures 3C and 3D), the O-O bond length elongates to 1.68 Å from 1.51 Å, whereas the O_1-H_2 distance contracts to 1.75 Å from 2.00 Å in the adsorbed state, indicating that the O-O bond cleavage and O-H bond formation tend to occur concurrently in the H_2O_2 dissociation step. The Cu site still coordinates to the O_2 atom strongly, with a bond length of 1.82 Å in the transient state (TS). In the dissociated state, a H_2O molecule is formed, which is H-bonded to the active O* species with the H_2-O_2 distance of 1.60 Å. Then, the formed active O* species over the Cu-N_2 site is ready to react with benzene to form phenol.

On the Cu_1-N_3/HCNS catalyst (see Figures 3E and 3F), the H_2O_2 molecule is still adsorbed over the Cu site, but the Cu-O interaction is weaker than that adsorption on the Cu-N_2 site, as evidenced by the longer distance of Cu-O_2 (2.58 Å) and the weaker binding energy of H_2O_2 (−0.52 eV, see Figure 3F). Although hydrogen bonds are formed between the H atoms of H_2O_2 and N atoms of the catalyst, we did not observe obvious activation of H_2O_2 upon adsorption on the Cu-N_3 site owing to the weak interaction with Cu, and the O-O bond length does not change compared with that in gas phase molecule. In the formation of active O* species, Cu interaction with the O_2 atom is still weak in the transition state, with the Cu-O_2 bond length of 2.20 Å. This bond length is 0.38 Å longer than that in the transition state generated over the Cu-N_2 site, indicating an unstable transition state for active O* formation over the Cu-N_3 site. Although the elementary pathways for H_2O_2 adsorption and dissociation are similar over Cu_1-N_2/HCNS and Cu_1-N_3/HCNS catalysts, the energy barrier of H_2O_2* dissociation to O* is up to 1.16 eV on the Cu-N_3 site, with an unfavorable reaction energy of 0.86 eV.

Comparing the energy pathways for H_2O_2 adsorption and dissociation on the two single-atom catalysts, clearly, the Cu_1-N_2/HCNS is catalytically more active for both H_2O_2 activation and active O* species formation, which would be a superior candidate for benzene oxidation than the Cu_1-N_3/HCNS catalyst.

To supplement the DFT results, the comparative trials were rationally designed and carried out (see Figure S9). The excess benzene versus H_2O_2 was used to ensure that the *in situ* formed active oxygen from H_2O_2 is rapidly consumed. The results indicate that Cu_1-N_2/HCNS shows a higher H_2O_2 activation rate with higher benzene conversion than Cu_1-N_3/HCNS catalyst, firmly demonstrating that the much higher activity of Cu_1-N_2/HCNS for selective oxidation of benzene compared with Cu_1-N_3/HCNS catalyst may originate from its higher H_2O_2 activation ability.

Kinetic Studies of Benzene Oxidation

To get further experimental insight into the much superior catalytic performance of the developed single-atom Cu_1-N_2/HCNS catalyst, kinetic studies of benzene oxidation were carried out in a kinetic controlled regime. From Figures 3G and S10 and Table S5, the two single-atom catalysts exhibit a lower apparent activation barrier (E_a) than that of supported nanocluster (Cu NC/HCNS) and nanoparticle (Cu NP/HCNS) catalysts for the benzene oxidation reaction. Moreover, the single atomic Cu_1-N_2/HCNS catalyst demonstrates much lower E_a and much higher pre-exponential factor (A) concerning benzene oxidation than Cu_1-N_3/HCNS, originating from the different properties of Cu-N_2 catalytic sites and Cu-N_3 moieties. As a consequence, the Cu_1-N_2/HCNS catalyst displays much higher *TON* for benzene selective oxidation to phenol in comparison with other catalysts (see Figure 3A and Table S4).

From the reaction results for selective oxidation of benzene shown in Table S4, the developed single atomic Cu_1-N_2/HCNS catalyst exhibits a much higher selectivity toward phenol than Cu NC/HCNS and

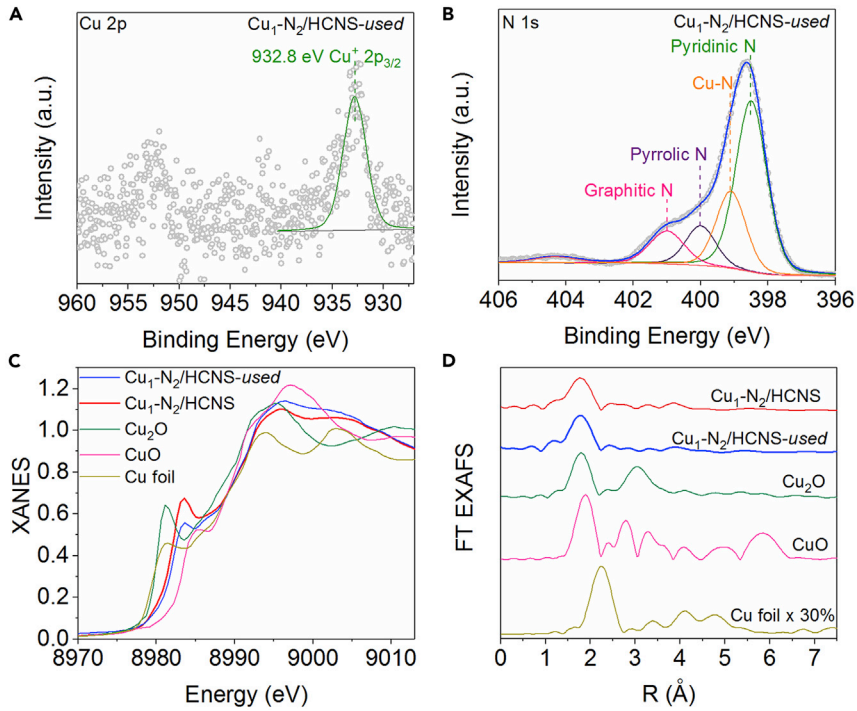

Figure 4. X-Ray Spectroscopy Analyses of the Used Single-Atom Catalyst

(A) Cu 2p XPS spectrum of Cu_1-N_2/HCNS-*used*.

(B) N 1s XPS spectrum of Cu_1-N_2/HCNS-*used*.

(C) Normalized Cu *K*-edge XANES spectra of Cu foil, CuO, Cu_2O, and Cu_1-N_2/HCNS-*used*.

(D) The k^3-weighted Fourier transform spectra from Cu *K*-edge EXAFS.

Cu NP/HCNS catalysts. From our previous finding (Zhang et al., 2018a, 2018b), quinone confirmed by mass spectrometry, as the detected by-product, possibly results from the deep oxidation of as-formed phenol over Cu_1-N_2/HCNS catalyst. Therefore, kinetic studies of phenol oxidation over Cu_1-N_2/HCNS, Cu NC/HCNS, and Cu NP/HCNS catalysts were carried out to explore the origin of the higher selectivity of Cu_1-N_2/HCNS than the other two. As shown in Figures 3H and S11, and Table S5, Cu_1-N_2/HCNS exhibits a slightly lower *A* than Cu NC/HCNS and Cu NP/HCNS for phenol oxidation to quinone, indicating the unfavorable for phenol oxidation. Furthermore, as shown as earlier, Cu_1-N_2/HCNS exhibits much lower *Ea* with much higher *A* for benzene oxidation than Cu NC/HCNS and Cu NP/HCNS (Table S5). As a consequence, Cu_1-N_2/HCNS exhibits much higher selectivity for hydroxylation of benzene to phenol than Cu NC/HCNS and Cu NP/HCNS catalysts.

In other words, the extremely higher activity of Cu_1-N_2/HCNS compared with Cu_1-N_3/HCNS originates from its much higher H_2O_2 activation and lower E_a with much higher *A* for benzene oxidation. The much higher phenol selectivity of Cu_1-N_2/HCNS compared with Cu NC/HCNS and Cu NP/HCNS derives from the much lower E_a with much higher *A* for benzene oxidation but the comparable E_a with slightly lower *A* for phenol oxidation to quinone.

The developed Cu_1-N_2/HCNS catalyst in this work shows high recycling stability and reusability. ICP and XPS results indicate the Cu content of the used catalyst is similar to that of the fresh catalyst (Table S6), demonstrating that the single Cu atoms are firmly anchored on HCNS owing to the strong coordination of Cu-N bond (see Figures 4A and 4B). More interestingly, the phenol selectivity increases from 91.5% to 97%–99% from the second cycle (see Figure 3B). The XANES profile of Cu_1-N_2/HCNS-*used* (see Figures 4C, 4D, and S12) determines a slight increase of oxidation state of Cu from +1.5 to +1.7 (see Table S3), correlating to the larger CN value of Cu-O from 0.9 to 1.4 via EXAFS fit, indicating the possible oxidation of Cu by H_2O_2 during the reaction process thus inducing the variation of local atomic structure of single-atom Cu. The increased phenol selectivity may result from the variation of the local atomic structure of

single Cu atom. To verify this hypothesis, the controlled experiment was performed. Figure 3B shows that the phenol selectivity increases to 97% over the H_2O_2 pretreated Cu_1-N_2/HCNS, firmly proving our aforementioned hypothesis. The developed Cu_1-N_2/HCNS catalyst shows outstanding catalytic performance for hydroxylation of benzene to phenol, and more than 70% of benzene conversion with close to 99% of phenol selectivity has been obtained.

Conclusions

In summary, we present a facile reduction deposition-acid leaching strategy for preparing the single atomic Cu_1-N_2/HCNS catalyst. Owing to the unique local atomic structure of Cu atom center, the single-atom Cu-N_2 catalytic sites are far superior to Cu-N_3 sites with the former showing 3.4 times higher *TON* for benzene hydroxylation to phenol compared with the latter under the same reaction conditions. Moreover, Cu_1-N_2/HCNS catalyst demonstrates much higher selectivity (close to 99%) and stability than Cu nanoparticles and nanoclusters. The unique Cu-N_2 sites anchored on the g-C_3N_4 surface are responsible for the outstanding catalytic properties concerning activity, selectivity, and stability for benzene hydroxylation to phenol, and the unique Cu-N_2 is extremely more active than Cu-N_3 owing to its much lower energy barrier regarding H_2O_2 activation owing to the unique coordination state of local atomic structure, confirmed by the results from experiments and DFT calculations. This work not only generates an efficient benzene hydroxylation catalyst for phenol production, but also presents a facile and efficient method for modulating coordination environment of single metallic atoms to design excellent catalysts.

Limitations of the Study

In this paper, we have proved that single-atom catalyst with Cu-N_2 sites shows extremely high activity than Cu-N_3 sites for benzene hydroxylation with H_2O_2 to phenol. However, our current evaluation system needs a large amount of H_2O_2 for a high benzene conversion, which results in a relatively low utilization of H_2O_2 because of its invalid decomposition.

METHODS

All methods can be found in the accompanying Transparent Methods supplemental file.

SUPPLEMENTAL INFORMATION

Supplemental Information can be found online at https://doi.org/10.1016/j.isci.2019.11.010.

ACKNOWLEDGMENTS

This work is financially supported by National Natural Science Foundation of China (21676046, U1610104). Dr. Guanghui Zhang is kindly acknowledged for his fruitful discussion on EXAFS.

AUTHOR CONTRIBUTIONS

T.Z. conceived and performed the experiments, collected and analyzed data, and wrote the paper. X.N. conducted the density functional theory calculation, analysis, and also wrote this section. W.Y. participated in the synthesis of materials. X.G. participated in the data analysis and discussions. C.S. participated in the data analysis and discussions and also revised the paper. R.S. performed XAS measurement and participated in the XAS data analysis and wrote this section. Y.L. conducted the HAADF-STEM studies. Z.Z. conceived the idea, supervised the project work, and led the data analysis and discussion, and prepared and finalized the paper. All the authors commented on the manuscript and have given approval to the final version of the manuscript.

DECLARATION OF INTERESTS

The authors declare no competing interests.

Received: August 16, 2019
Revised: October 22, 2019
Accepted: November 4, 2019
Published: December 20, 2019

REFERENCES

Acharyya, S.S., Ghosh, S., and Bal, R. (2014). Fabrication of three-dimensional (3D) raspberry-like copper chromite spinel catalyst in a facile hydrothermal route and its activity in selective hydroxylation of benzene to phenol. ACS Appl. Mater. Interfaces *6*, 14451–14459.

Bal, R., Tada, M., Sasaki, T., and Iwasawa, Y. (2006). Direct phenol synthesis by selective oxidation of benzene with molecular oxygen on an interstitial-N/Re cluster/zeolite catalyst. Angew. Chem. Int. Ed. *45*, 448–452.

Balducci, L., Bianchi, D., Bortolo, R., D'Aloisio, R., Ricci, M., Tassinari, R., and Ungarelli, R. (2003). Direct oxidation of benzene to phenol with hydrogen peroxide over a modified titanium silicalite. Angew. Chem. Int. Ed. *42*, 4937–4940.

bin Mohd Yusoff, A.R., Kim, D., Schneider, F.K., da Silva, W.J., and Jang, J. (2015). Au-doped single layer graphene nanoribbons for a record-high efficiency ITO-free tandem polymer solar cell. Energy Environ. Sci. *8*, 1523–1537.

Chen, X., Zhang, J., Fu, X., Antonietti, M., and Wang, X. (2009). Fe-g-C_3N_4-Catalyzed oxidation of benzene to phenol using hydrogen peroxide and visible light. J. Am. Chem. Soc. *131*, 11658–11659.

Chen, Z., Vorobyeva, E., Mitchell, S., Fako, E., Ortuño, M.A., López, N., Collins, S.M., Midgley, P.A., Richard, S., Vilé, G., and Pérez-Ramírez, J. (2018a). A heterogeneous single-atom palladium catalyst surpassing homogeneous systems for Suzuki coupling. Nat. Nanotechnol. *13*, 702–707.

Chen, Y., Ji, S., Chen, C., Peng, Q., Wang, D., and Li, Y. (2018b). Single-atom catalysts: synthetic strategies and electrochemical applications. Joule *2*, 1242–1264.

Cheng, C., Li, S., Xia, Y., Ma, L., Nie, C., Roth, C., Thomas, A., and Haag, R. (2018). Atomic Fe–N_x coupled open-mesoporous carbon nanofibers for efficient and bioadaptable oxygen electrode in Mg–air batteries. Adv. Mater. *30*, 1802669.

Deng, D., Chen, X., Yu, L., Wu, X., Liu, Q., Liu, Y., Yang, H., Tian, H., Hu, Y., Du, P., et al. (2015). A single iron site confined in a grapheme matrix for the catalytic oxidation of benzene at room temperature. Sci. Adv. *1*, e1500462.

Di, Y., Wang, X., Thomas, A., and Antonietti, M. (2010). Making metal-carbon nitride heterojunctions for improved photocatalytic hydrogen evolution with visible light. ChemCatChem *2*, 834–838.

Dvořák, F., Camellone, M.F., Tovt, A., Tran, N.-D., Negreiros, F.R., Vorokhta, M., Skála, T., Matolínová, I., Mysliveček, J., Matolín, V., and Fabris, S. (2016). Creating single-atom Pt-ceria catalysts by surface step decoration. Nat. Commun. *7*, 10801.

ElMetwally, A.E., Eshaq, G., Yehia, F.Z., Al-Sabagh, A.M., and Kegnæs, S. (2018). Iron oxychloride as an efficient catalyst for selective hydroxylation of benzene to phenol. ACS Catal. *8*, 10668–10675.

Evtushok, V.Y., Suboch, A.N., Podyacheva, O.Y., Stonkus, O.A., Zaikovskii, V.I., Chesalov, Y.A., Kibis, L.S., and Kholdeeva, O.A. (2018). Highly efficient catalysts based on divanadium-substituted polyoxometalate and N-doped carbon nanotubes for selective oxidation of alkylphenols. ACS Catal. *8*, 1297–1307.

Frenkel, A.I., Wang, Q., Marinkovic, N., Chen, J.G., Barrio, L., Si, R., Camara, A.L., Estrella, A.M.J., Rodriguez, A., and Hanson, J.C. (2011). Combining X-ray absorption and X-ray diffraction techniques for in situ studies of chemical transformations in heterogeneous catalysis: advantages and limitations. J. Phys. Chem. C *115*, 17884–17890.

Gao, G., Jiao, Y., Waclawik, E.R., and Du, A. (2016). Single atom (Pd/Pt) supported on graphitic carbon nitride as an efficient photocatalyst for visible-light reduction of carbon dioxide. J. Am. Chem. Soc. *138*, 6292–6297.

Han, J., Jung, J., Lee, Y., Nam, W., and Fukuzumi, S. (2017). Photocatalytic oxidation of benzene to phenol using dioxygen as an oxygen source and water as an electron source in the presence of a cobalt catalyst. Chem. Sci. *8*, 7119–7125.

Han, Y., Wang, Y., Xu, R., Chen, W., Zheng, L., Han, A., Zhu, Y., Zhang, J., Zhang, H., Luo, J., et al. (2018). Electronic structure engineering to boost oxygen reduction activity by controlling the coordination of the central metal. Energy Environ. Sci. *11*, 2348–2352.

Harmer, M.A., Farneth, W.E., and Sun, Q. (1996). High surface area nafion resin/silica nanocomposites: a new class of solid acid catalyst. J. Am. Chem. Soc. *118*, 7708–7715.

Hosseini, S.M., Ghiaci, M., Kulinich, S.A., Wunderlich, W., Farrokhpour, H., Saraji, M., and Shahvar, A. (2018). Au-Pd@g-C_3N_4 as an efficient photocatalyst for visible-light oxidation of benzene to phenol: experimental and mechanistic study. J. Phys. Chem. C *122*, 27477–27485.

Ivanchikova, I.D., Maksimchuk, N.V., Maksimovskaya, R.I., Maksimov, G.M., and Kholdeeva, O.A. (2014). Highly selective oxidation of alkylphenols to *p*-benzoquinones with aqueous hydrogen peroxide catalyzed by divanadium-substituted polyoxotungstates. ACS Catal. *4*, 2706–2713.

Jiang, K., Siahrostami, S., Zheng, T., Hu, Y., Hwang, S., Stavitski, E., Peng, Y., Dynes, J., Gangisetty, M., Su, D., et al. (2018). Isolated Ni single atoms in graphene nanosheets for high-performance CO_2 reduction. Energy Environ. Sci. *11*, 893–903.

Jun, Y., Park, J., Lee, S.U., Thomas, A., Hong, W.H., and Stucky, G.D. (2013a). Three-dimensional macroscopic assemblies of low-dimensional carbon nitrides for enhanced hydrogen evolution. Angew. Chem. Int. Ed. *52*, 11083–11087.

Jun, Y., Lee, E.Z., Wang, X., Hong, W.H., Stucky, G.D., and Thomas, A. (2013b). From melamine-cyanuric acid supramolecular aggregates to carbon nitride hollow spheres. Adv. Funct. Mater. *23*, 3661–3667.

Kau, L.S., Spira-Solomon, D.J., Penner-Hahn, J.E., Hodgson, K.O., and Solomon, E.I. (1987). X-ray absorption edge determination of the oxidation state and coordination number of copper: application to the type 3 site in *Rhus vernicifera* lacease and its reaction with oxygen. J. Am. Chem. Soc. *109*, 6433–6442.

Kwon, Y., Kim, T.Y., Kwon, G., Yi, J., and Lee, H. (2017). Selective activation of methane on single-atom catalyst of rhodium dispersed on zirconia for direct conversion. J. Am. Chem. Soc. *139*, 17694–17699.

Labinger, J.A., and Bercaw, J.E. (2002). Understanding and exploiting C-H bond activation. Nature *417*, 507–514.

Leitch, J.A., and Frost, C.G. (2017). Ruthenium-catalysed activation for remote *meta*-selective C–H functionalization. Chem. Soc. Rev. *46*, 7145–7153.

Li, F., Han, G., Noh, H., Kim, S., Lu, Y., Jeong, H.Y., Fu, Z., and Baek, J. (2018a). Boosting oxygen reduction catalysis with abundant copper single atom active sites. Energy Environ. Sci. *11*, 2263–2269.

Li, Y., Liu, X., Zhang, Z., Zhao, S., Tian, G., Zheng, J., Wang, D., Shi, S., and Russell, T.P. (2018b). Adaptive structured pickering emulsions and porous materials based on cellulose nanocrystal surfactants. Angew. Chem. Int. Ed. *57*, 13560–13564.

Liang, H., Brüller, S., Dong, R., Zhang, J., Feng, X., and Müllen, K. (2015). Molecular metal–N_x centres in porous carbon for electrocatalytic hydrogen evolution. Nat. Commun. *6*, 7992.

Liu, J., Wang, H., and Antonietti, M. (2016). Graphitic carbon nitride "Reloaded": emerging applications beyond (photo) catalysis. Chem. Soc. Rev. *45*, 2308–2326.

Liu, W., Zhang, L., Liu, X., Liu, X., Yang, X., Miao, S., Wang, W., Wang, A., and Zhang, T. (2017). Discriminating catalytically active FeN_x species of atomically dispersed Fe-N-C catalyst for selective oxidation of the C-H bond. J. Am. Chem. Soc. *139*, 10790–10798.

Liu, W., Chen, Y., Qi, H., Zhang, L., Yan, W., Liu, X., Yang, X., Miao, S., Wang, W., Liu, C., et al. (2018). A durable nickel single-atom catalyst for hydrogenation reactions and cellulose valorization under harsh conditions. Angew. Chem. Int. Ed. *57*, 7071–7075.

Malonzo, C.D., Shaker, S.M., Ren, L., Prinslow, S.D., Platero-Prats, A.E., Gallington, L.C., Borycz, J., Thompson, A.B., Wang, T.C., Farha, O.K., et al. (2016). Thermal stabilization of metal–organic framework-derived single-site catalytic clusters through nanocasting. J. Am. Chem. Soc. *138*, 2739–2748.

Marcinkowski, M.D., Darby, M.T., Liu, J., Wimble, J.M., Lucci, F.R., Lee, S., Michaelides, A., Flytzani-Stephanopoulos, M., Stamatakis, M., and Sykes, E.C.H. (2018). Pt/Cu single-atom alloys as coke-resistant catalysts for efficient C–H activation. Nat. Chem. *10*, 325–332.

Matei, F., Jiménez-Borja, C., Canales-Vázquez, J., Brosda, S., Dorado, F., Valverde, J.L., and Ciuparu, D. (2013). Enhanced electropromotion of methane combustion on palladium catalysts

deposited on highly porous supports. Appl. Catal. B Environ. *132-133*, 80–89.

Mitchell, S., Vorobyeva, E., and Pérez-Ramírez, J. (2018). The multifaceted reactivity of single-atom heterogeneous catalysts. Angew. Chem. Int. Ed. *57*, 15316–15329.

Morimoto, Y., Bunno, S., Fujieda, N., Sugimoto, H., and Itoh, S. (2015). Direct hydroxylation of benzene to phenol using hydrogen peroxide catalyzed by nickel complexes supported by pyridylalkylamine ligands. J. Am. Chem. Soc. *137*, 5867–5870.

Qiao, B., Wang, A., Yang, X., Allard, L.F., Jiang, Z., Cui, Y., Liu, J., Li, J., and Zhang, T. (2011). Single-atom catalysis of CO oxidation using Pt_1/FeO_x. Nat. Chem. *3*, 634–641.

Qu, Y., Li, Z., Chen, W., Lin, Y., Yuan, T., Yang, Z., Zhao, C., Wang, J., Zhao, C., Wang, X., et al. (2018). Direct transformation of bulk copper into copper single sites via emitting and trapping of atoms. Nat. Catal. *1*, 781–786.

Sambiagio, C., Schönbauer, D., Blieck, R., Dao-Huy, T., Pototschnig, G., Schaaf, P., Wiesinger, T., Zia, M.F., Wencel-Delord, J., Besset, T., et al. (2018). Comprehensive overview of directing groups applied in metal-catalysed C–H functionalisation. Chem. Soc. Rev. *47*, 6603–6743.

Shan, C., Zhu, L., Qu, L., Bai, R., and Lan, Y. (2018). Mechanistic view of Ru-catalyzed C–H bond activation and functionalization: computational advances. Chem. Soc. Rev. *47*, 7552–7576.

Shilov, A.E., and Shul'pin, G.B. (1997). Activation of C-H bonds by metal complexes. Chem. Rev. *97*, 2879–2932.

Sorrell, T.N., and Malachowski, M.R. (1983). Mononuclear three-coordinate copper (I) complexes: synthesis, structure, and reaction with carbon monoxide. Inorg. Chem. *22*, 1883–1887.

Sorrell, T.N., Malachowski, M.R., and Jameson, D.L. (1982). Synthesis, structure, and reactivity of a binuclear three-coordinate copper (I) complex. Inorg. Chem. *21*, 3250–3252.

Su, Y., Han, Z., Zhang, L., Wang, W., Duan, M., Li, X., Zheng, Y., Wang, Y., and Lei, X. (2017). Surface hydrogen bonds assisted mesoporous WO_3 photocatalysts for high selective oxidation of benzylalcohol to benzylaldehyde. Appl. Catal. B Environ. *217*, 108–114.

Szécsényi, Á., Li, G., Gascon, J., and Pidko, E.A. (2018). Mechanistic complexity of methane oxidation with H_2O_2 by single-site Fe/ZSM-5 catalyst. ACS Catal. *8*, 7961–7972.

Thomas, J.M., Raja, R., and Lewis, D.W. (2005). Single-site heterogeneous catalysts. Angew. Chem. Int. Ed. *44*, 6456–6482.

Tsuji, T., Zaoputra, A.A., Hitomi, Y., Mieda, K., Ogura, T., Shiota, Y., Yoshizawa, K., Sato, H., and Kodera, M. (2017). Specific enhancement of catalytic activity by a dicopper core: selective hydroxylation of benzene to phenol with hydrogen peroxide. Angew. Chem. Int. Ed. *56*, 7779–7782.

Wang, Y., Wang, X., and Antonietti, M. (2012). Polymeric graphitic carbon nitride as a heterogeneous organocatalyst: from photochemistry to multipurpose catalysis to sustainable chemistry. Angew. Chem. Int. Ed. *51*, 68–89.

Wang, D., Wang, M., and Li, Z. (2015). Fe-based metal-organic frameworks for highly selective photocatalytic benzene hydroxylation to phenol. ACS Catal. *5*, 6852–6857.

Wencel-Delord, J., and Glorius, F. (2013). C-H bond activation enables the rapid construction and late-stage diversifcation of functional molecules. Nat. Chem. *5*, 369–375.

Xia, Y., and Tang, Z. (2012). Monodisperse hollow supraparticles via selective oxidation. Adv. Funct. Mater. *22*, 2585–2593.

Xu, J., Chen, Y., Hong, Y., Zheng, H., Ma, D., Xue, B., and Li, Y. (2018). Direct catalytic hydroxylation of benzene to phenol catalyzed by vanadia supported on exfoliated graphitic carbon nitride. Appl. Catal. Gen. *549*, 31–39.

Yamaguchi, S., Kamiya, K., Hashimoto, K., and Nakanishi, S. (2017). Ru atom-modified covalent triazine framework as a robust electrocatalyst for selective alcohol oxidation in aqueous electrolytes. Chem. Commun. (Camb.) *53*, 10437–10440.

Yamaguchi, S., Suzuki, A., Togawa, M., Nishibori, M., and Yahiro, H. (2018). Selective oxidation of thioanisole with hydrogen peroxide using copper complexes encapsulated in zeolite: formation of a thermally stable and reactive copper hydroperoxo species. ACS Catal. *8*, 2645–2650.

Yamashita, H., Mori, K., Kuwahara, Y., Kamegawa, T., Wen, M., Verma, P., and Che, M. (2018). Single-site and nano-confined photocatalysts designed in porous materials for environmental uses and solar fuels. Chem. Soc. Rev. *47*, 8072–8096.

Yang, J., Sun, G., Gao, Y., Zhao, H., Tang, P., Tan, J., Lu, A., and Ma, D. (2013). Direct catalytic oxidation of benzene to phenol over metal-free graphene-based catalyst. Energy Environ. Sci. *6*, 793–798.

Yang, S., Kim, J., Tak, Y.J., Soon, A., and Lee, H. (2016). Single-atom catalyst of platinum supported on titanium nitride for selective electrochemical reactions. Angew. Chem. Int. Ed. *55*, 2058–2062.

Yuan, J., Zhang, W., Li, X., and Yang, J. (2018). A high performance catalyst for methane conversion to methanol: graphene supported single atom Co. Chem. Commun. (Camb.) *54*, 2284–2287.

Zhang, M., Wang, Y., Chen, W., Dong, J., Zheng, L., Luo, J., Wan, J., Tian, S., Cheong, W., Wang, D., and Li, Y. (2017a). Metal (Hydr) oxides@Polymer core-shell strategy to metal single atom materials. J. Am. Chem. Soc. *139*, 10976–10979.

Zhang, H., Hwang, S., Wang, M., Feng, Z., Karakalos, S., Luo, L., Qiao, Z., Xie, X., Wang, C., Su, D., et al. (2017b). Single atomic iron catalysts for oxygen reduction in acidic media: particle size control and thermal activation. J. Am. Chem. Soc. *139*, 14143–14149.

Zhang, X., Sun, Z., Wang, B., Tang, Y., Nguyen, L., Li, Y., and Tao, F.F. (2018a). C-C coupling on single-atom-based heterogeneous catalyst. J. Am. Chem. Soc. *140*, 954–962.

Zhang, T., Zhang, D., Han, X., Dong, T., Guo, X., Song, C., Si, R., Liu, W., Liu, Y., and Zhao, Z. (2018b). Preassembly strategy to fabricate porous hollow carbonitride spheres inlaid with single Cu-N_3 sites for selective oxidation of benzene to phenol. J. Am. Chem. Soc. *140*, 16936–16940.

Zhao, Z., Ge, G., and Zhang, D. (2018). Heteroatom-doped carbonaceous photocatalysts for solar fuel production and environmental remediation. ChemCatChem *10*, 62–123.

Zhu, Y., Sun, W., Luo, J., Chen, W., Cao, T., Zheng, L., Dong, J., Zhang, J., Zhang, M., Han, Y., et al. (2018). A cocoon silk chemistry strategy to ultrathin N-doped carbon nanosheet with metal single-site catalysts. Nat. Commun. *9*, 3861–3869.

ISCI, Volume *22*

Supplemental Information

Single Atomic Cu-N_2 Catalytic Sites for Highly Active and Selective Hydroxylation of Benzene to Phenol

Ting Zhang, Xiaowa Nie, Weiwei Yu, Xinwen Guo, Chunshan Song, Rui Si, Yuefeng Liu, and Zhongkui Zhao

Supporting Information

Supplemental Data Items

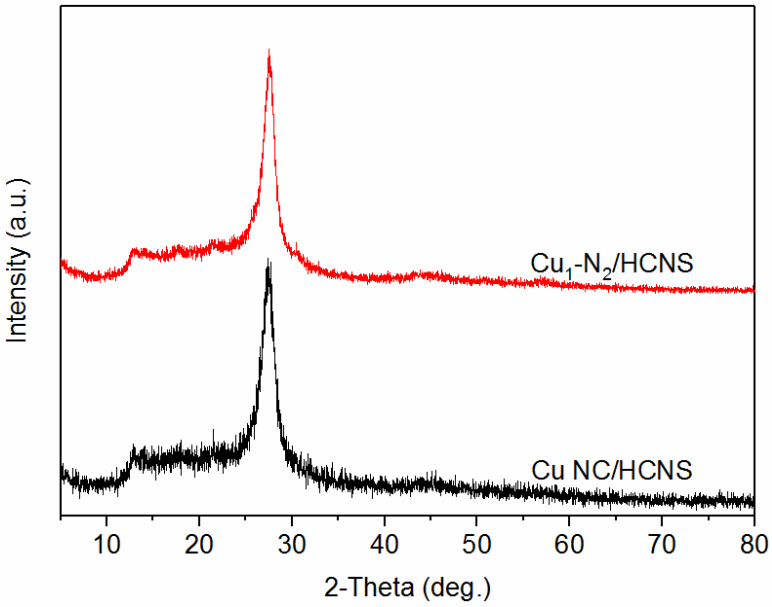

Figure S1. The XRD Patterns of Cu NC/HCNS and Cu_1-N_2/HCNS, related to Figure 1.

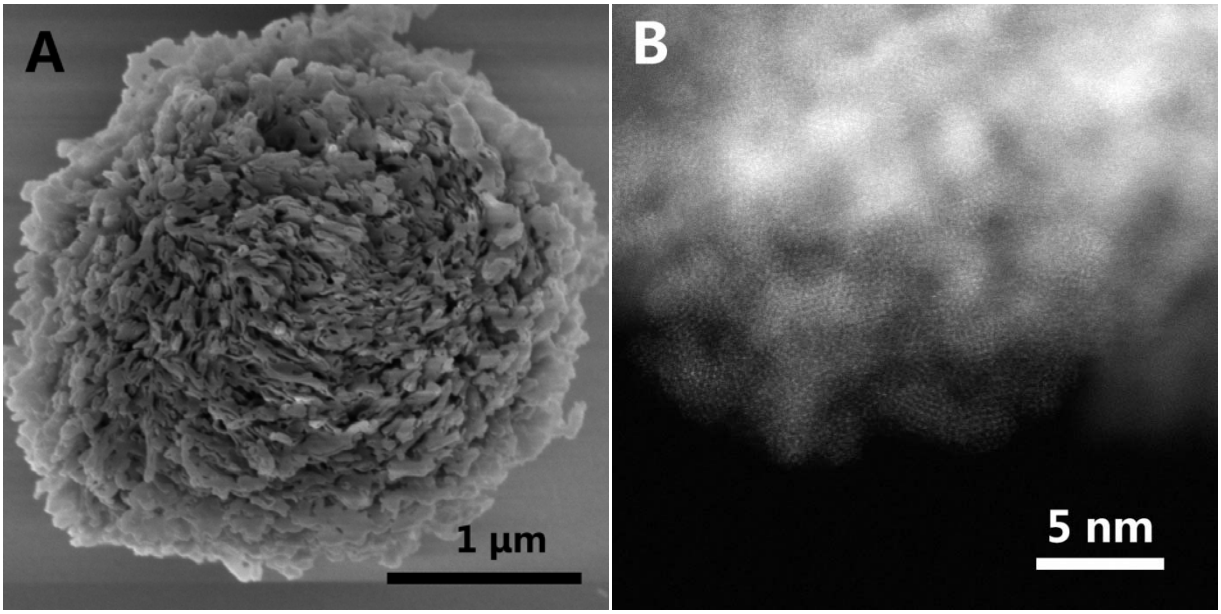

Figure S2. (A) SEM Image of Single-atom Cu_1-N_2/HCNS Catalyst and (B) HAADF-STEM image of Cu NC/HCNS, related to Figure 1.

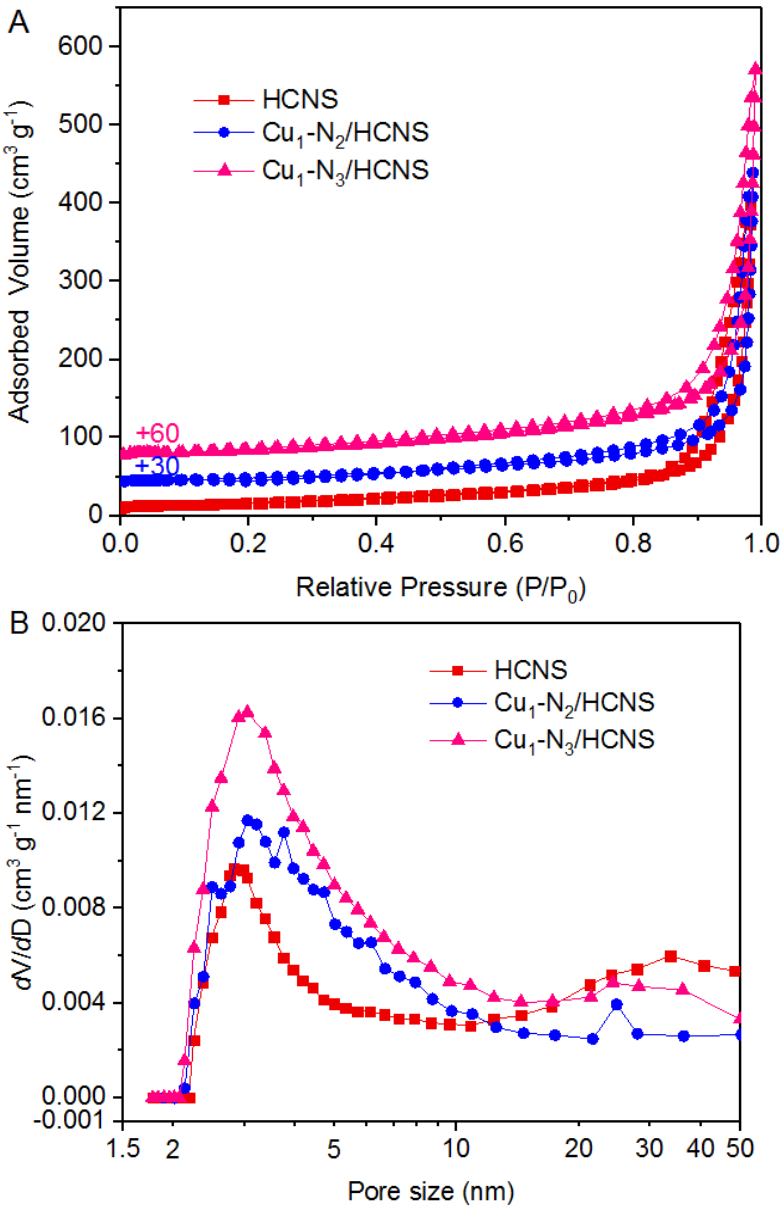

Figure S3. Nitrogen Physisorption Analysis of Single-atom Cu_1-N_2/HCNS Catalyst, Cu_1-N_3/HCNS Catalyst and HCNS Support, related to Figure 1.

(A) Isotherms curves

(B) Pore size distribution curves

Table S1. Textural Properties of Single-atom Cu_1-N_2/HCNS Catalyst and HCNS Support, related to Figure 1.

Entry	Sample	S_{BET} ($m^2 \cdot g^{-1}$)	V_{BJH} ($cm^3 \cdot g^{-1}$)	V_{Total} ($cm^3 \cdot g^{-1}$)
1	HCNS	57	0.64	0.64
2	Cu_1-N_2/HCNS	65	0.67	0.67
3	Cu_1-N_3/HCNS	84	0.82	0.82

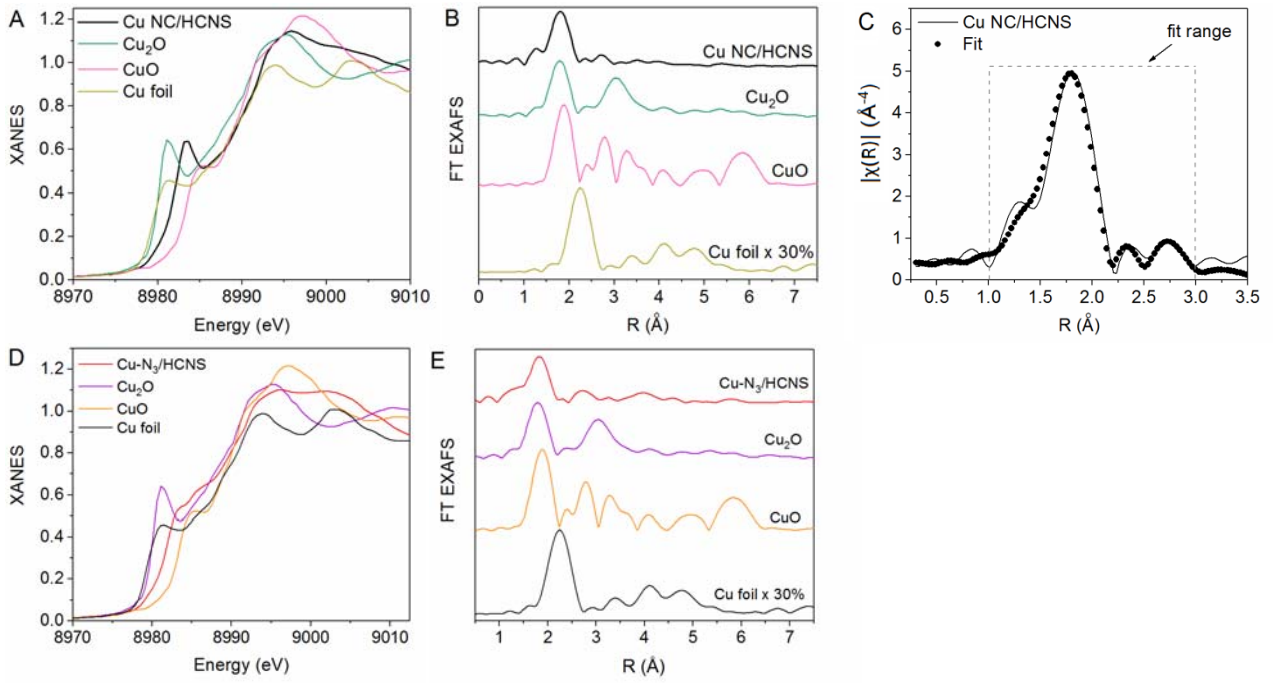

Figure S4. XAFS Analysis, related to Figure 1.
(A) Normalized Cu K-edge XANES spectra of Cu foil, CuO, Cu_2O and Cu NC/HCNS.
(B) The k^3-weighted Fourier transform spectra from Cu K-edge EXAFS.
(C) The corresponding EXAFS fitting curve of Cu NC/HCNS.
(D) Normalized Cu K-edge XANES spectra of Cu foil, CuO, Cu_2O and Cu_1-N_3/HCNS.
(E) The k^3-weighted Fourier transform spectra from Cu K-edge EXAFS of Cu foil, CuO, Cu_2O and Cu_1-N_3/HCNS.

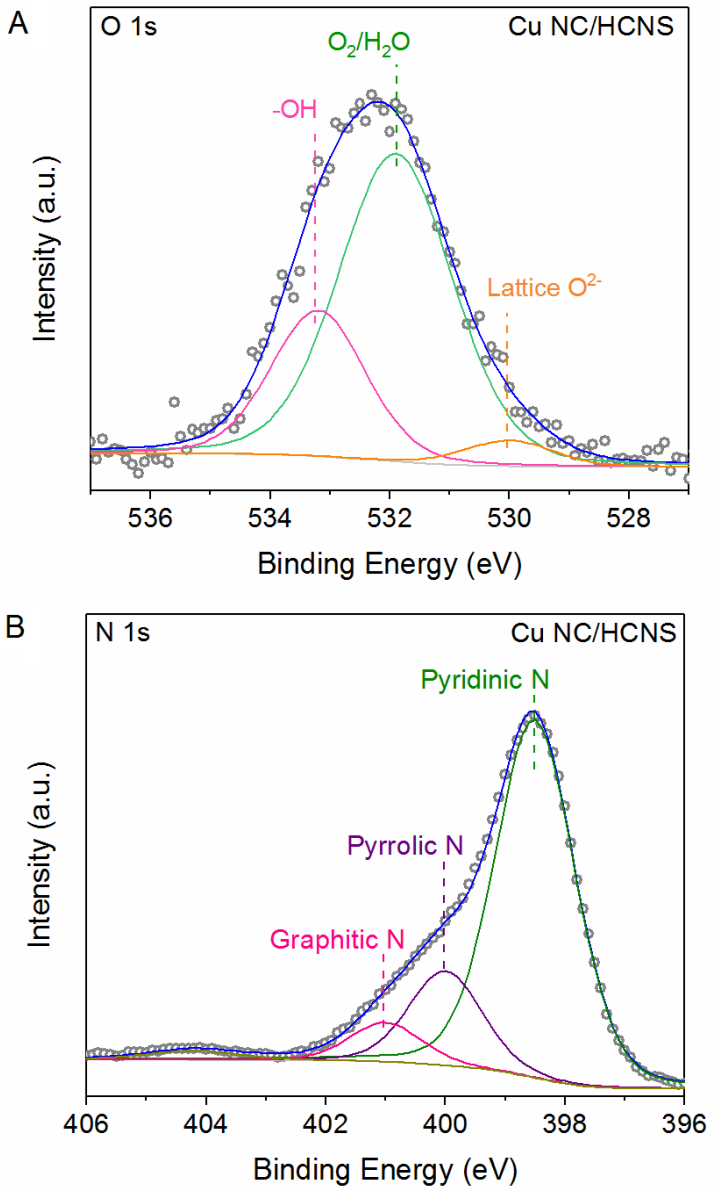

Figure S5. XPS analysis of Cu NC/HCNS catalyst, related to Figure 1.
(A) O 1s XPS spectrum.
(B) N 1s XPS spectrum.

Table S2. EXAFS fitting data for Cu NC/HCNS catalyst, related to Figure 1.

Sample	Cu-N (O)		Cu-Cu		σ^2 (Å^2)[c]	ΔE_0[d] (eV)	Valence
	R (Å)[a]	CN[b]	*R* (Å)[a]	CN[b]			
Cu NC/HCNS	1.92±0.01(O)	2.9±0.3(O)	2.87±0.04	0.4±0.2	0.007±0.001(N,O) 0.010± 0.006(Cu)	7.6±0.9	+1.6
Cu_1-N_3/HCNS[e]	1.96±0.01(N)	3.3±0.3(N)	-	-	0.007±0.001(N)	10.8±1.3	+1.6

[a]Bond distance;
[b]Coordination number;
[c]Debye-Waller factor;
[d]Inner potential dorrection.
[e]Cited from *Ref.* (Zhang et al., 2018)

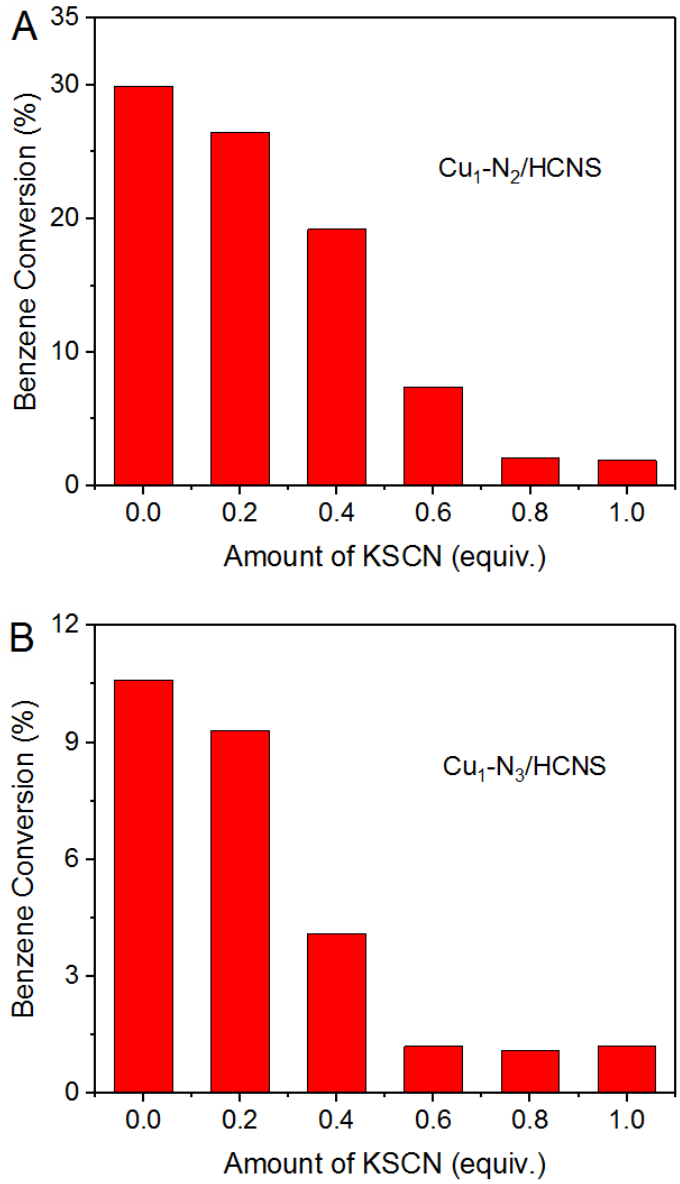

Figure S6. KSCN titration for determining the amount of active Cu sites, related to Figure 1.
Before the reaction carried out, single-atom catalyst was treated with certain amount of KSCN in water solution for 2 h. The amount of KSCN was calculated according to the total Cu content from ICP result. The following reaction was performed under following conditions: benzene (0.4 mL), H_2O_2 (6 mL) and acetonitrile (3 mL), 60 ^{o}C for 0.5 h.

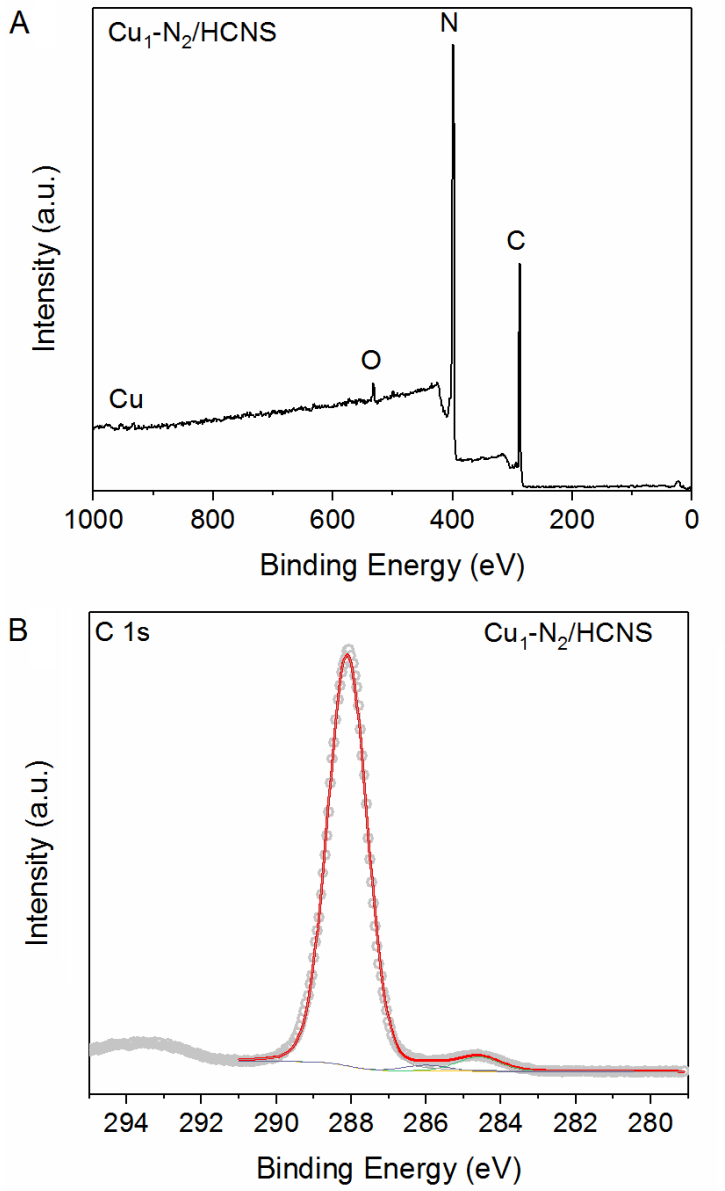

Figure S7. XPS analysis of Cu_1-N_2/HCNS catalyst, related to Figure 2.
(A) The survey XPS spectrum.
(B) The C 1s XPS spectrum.

Table S3. EXAFS fitting data for the fresh and used Cu_1-N_2/HCNS single-atom catalyst, related to Figure 2 and Figure 4.

Sample	Cu-N/O		Cu-Cu		σ^2 (Å^2)[c]	ΔE_0[d] (eV)	Valence
	R (Å)[a]	CN[b]	R (Å)[a]	CN[b]			
Cu_1-N_2/HCNS	1.92±0.03(N) 1.96±0.05(O)	2.0(N) 0.9±0.4(O)	-	-	0.007±0.001(N,O)	7.6±0.9	+1.5
Cu_1-N_2/HCNS-*used*[e]	1.94±0.07(N) 1.97±0.07(O)	2.0(N) 1.4±1.0(O)	-	-			+1.7

[a]Bond distance.

[b]Coordination number.

[c]Debye-Waller factor.

[d]Inner potential correction.

[e]The sample was recovered after one reaction cycle.

Table S4. Catalytic Performance of Various Catalysts for Direct Hydroxylation of Benzene to Phenol, related to Figure 3.

Entry	Sample	Temp. (°C)	Time (h)	Conv. (%)		*TON* of Benzen	*Sel.* (%)			Utilization of H_2O_2	Ref.
				Benzene	H_2O_2		Phenol	*p*-benzoquinone	others		
1[a]	Blank	60	12	1.5	-	-	>99.9	-	-	-	
2[a]	HCNS	60	12	5.2	-	-	>99.9	-	-	-	
3[a]	Cu_1-N_2/HCNS	60	2.5	70.9	47.3	6935	91.1	8.9	<0.1	15	This work
4[a]	Cu_1-N_3/HCNS	60	2.5	15.6	11.6	2034	99.3	0.7	<0.1	14	
5[a]	Cu NC/HCNS	60	2.5	44.7	25.5	3489	73.0	27.0	<0.1	16	
6[a]	Cu NP/HCNS	60	2.5	41.4	-	3231	70.9	29.1	<0.1	-	
7[a]	Cu_1-N_2/HCNS	60	12	76.8	-	-	91.5	8.5	<0.1	-	This work
8[b]	Cu_1-N_2/HCNS	60	3.5	89.3	-	2783	90.5	9.5	<0.1	-	This work
9[b]	Co-ISA/CNS	60	24	82.0	-	<722	86.0	-	-	-	Zhu er al., 2018
10	$[Ni(tepa)]^{2+}$	60	216	7.5	-	749	99.0	-	-	-	Morimoto, 2015
11[a]	SA-Fe/CN	60	24	45	-	786	94.0	-	-	-	Zhang et al., 2017
12[b]	Cu_1-N_2/HCNS	25	24	81.2	-	2531	86.6	13.4	<0.1	-	This work
13[b]	Co-ISA/CNS	25	24	53.0	-	<511	93.0	-	-	-	Zhu et al., 2018
14[b]	FeN_4/GN-2.7	25	24	23.4	-	44	80.0	-	-	-	Zhang et al., 2017

[a]Reaction conditions: 0.013 mol% active copper, molar ratio of H_2O_2 to substrate is 10:1, 0.5 mL of benzene, 6 mL of CH_3CN.

[b]Reaction conditions: 50.0 mg catalyst, 0.4 mL benzene, 6 mL H_2O_2 (30 wt%), 3 mL CH_3CN.

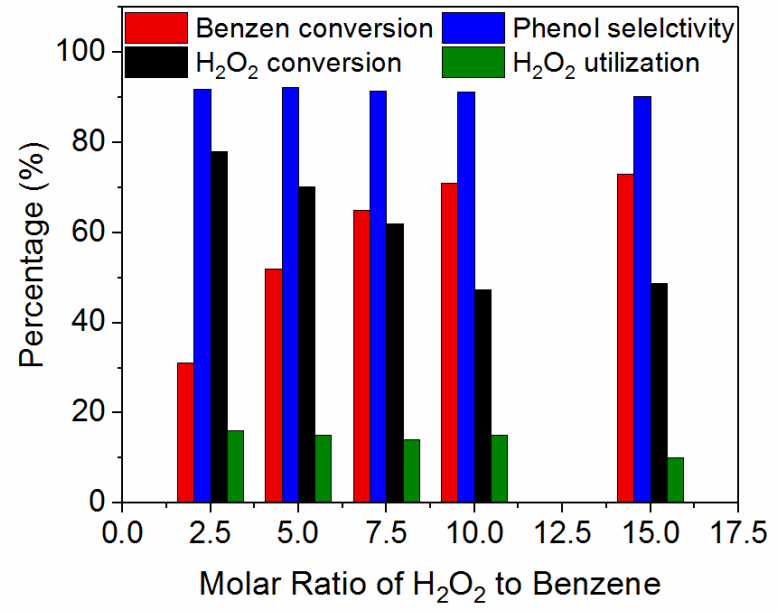

Figure S8. Effect of the Molar Ratio of H_2O_2 to Benzene in Benzene Oxidation over Cu_1-N_2/HCNS Catalsyt, related to Figure 3.

Reaction conditions: 20 mg catalyst, 0.5 mL benzene, 6 mL CH_3CN, and different amount of H_2O_2 (30%) at 60 ^oC for 2.5 h.

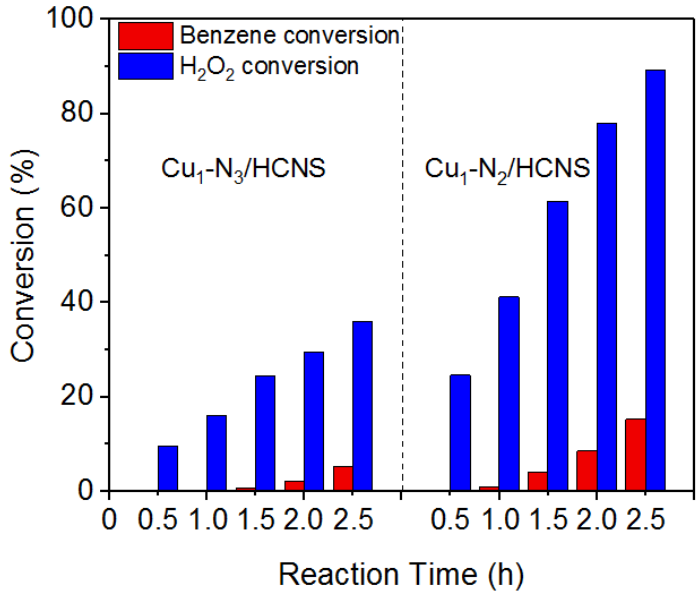

Figure S9. Comparative Trials for H_2O_2 Decomposition in Benzene Oxidation over Cu_1-N_2/HCNS Catalyst, related to Figure 3.

Reaction conditions: 0.0065 mol% active copper, 1.0 mL benzene (11 mmol), 0.52 mL H_2O_2 (30%) (5.5 mmol), and 6 mL CH_3CN at 60 ^oC.

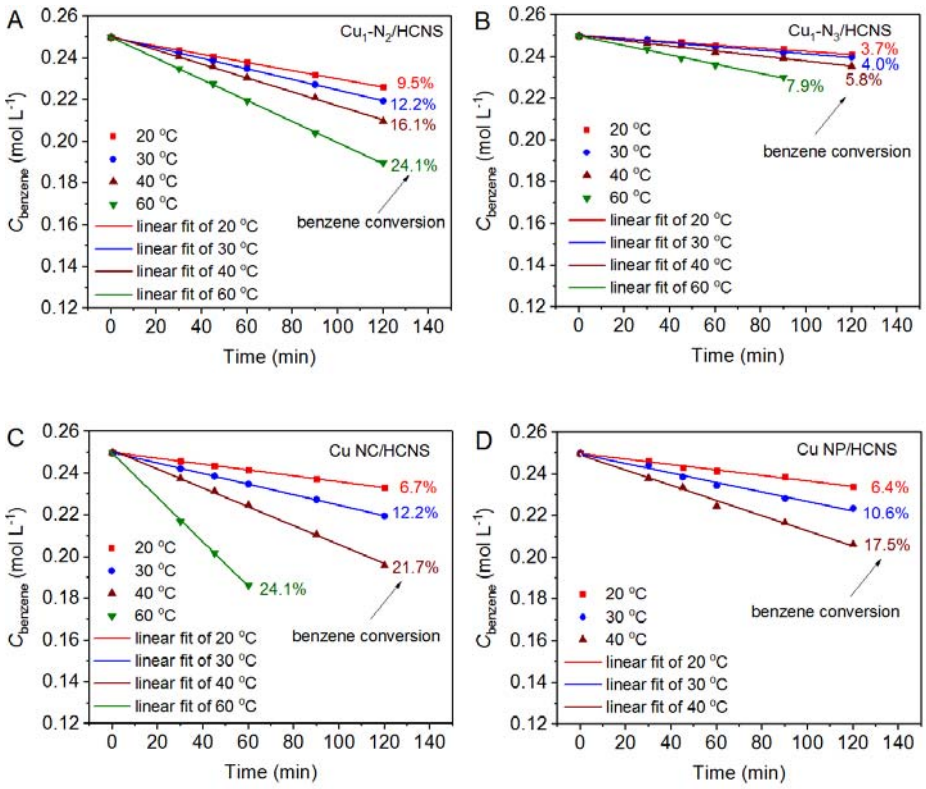

Figure S10. The Kinetic Data Concerning Variation of Benzene Concentration as a Function of Reaction Time at Different Temperatures in the Kinetic Controlled Regime, related to Figure 3.

Reaction conditions: 20 mg of Cat., 0.20 mL of benzene, 3.0 mL of H_2O_2 (30 wt%), 6 mL of CH_3CN. The data of Cu_1-N_3/HCNS and Cu NP/HCNS is cited from *Ref.* (Zhang et al., 2018).

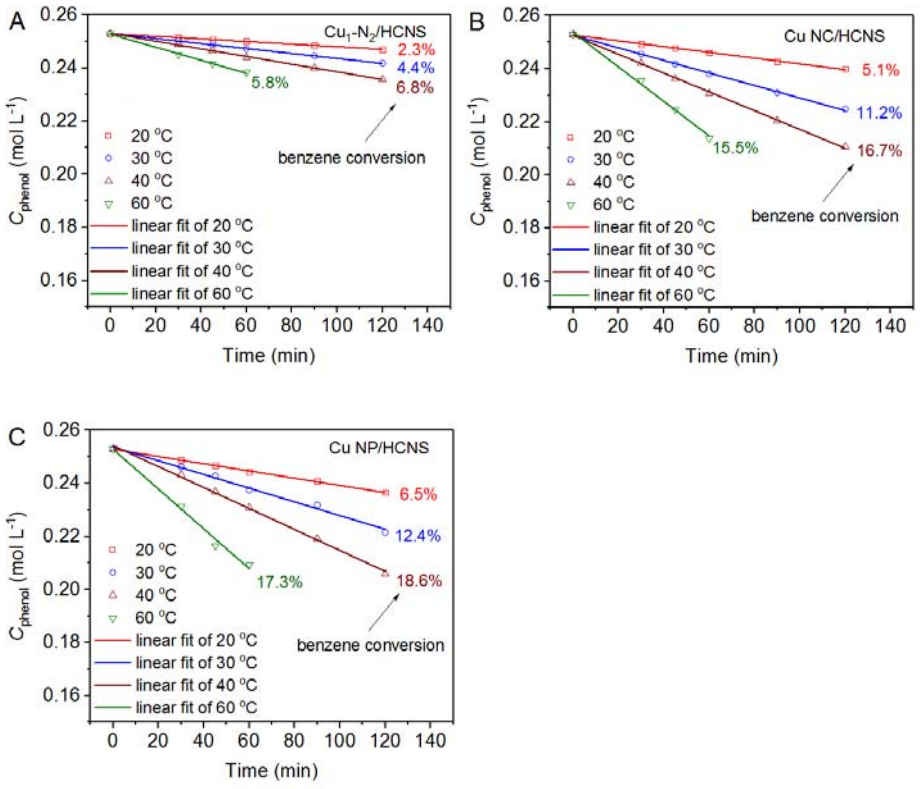

Figure S11. The Kinetic Data Concerning Variation of Phenol Concentration as a Function of Reaction Time at Different Temperatures in the Kinetic Controlled Regime, related to Figure 3. Reaction conditions: 20 mg of Cat., 0.20 mL of phenol, 3.0 mL of H_2O_2 (30 wt%), 6 mL of CH_3CN. The data of Cu NP/HCNS is cited from *Ref.* (Zhang et al., 2018).

Table S5. The Comparison of Kinetic Parameters of Benzene Oxidation and Phenol Oxidation over Various Catalysts, related to Figure 3.

Reaction	E_a (kJ mol^{-1})				$A_{Cu1\text{-}N3/HCNS}$/ $A_{Cu1\text{-}N2/HCNS}$	$A_{Cu\ NC/HCNS}$/ $A_{Cu1\text{-}N2/HCNS}$	$A_{Cu\ NP/HCNS}$/ $A_{Cu1\text{-}N2/HCNS}$
	Cu_1-N_2/HCNS	Cu_1-N_3/HCNS[a]	Cu NC/HCNS	Cu NP/HCNS[a]			
Benzene oxidation	18	27	52	53	1/8.0	1/1.4	1/1.2
Phenol oxidation	31	40	35	34	-	1.2/1	1.1/1

[a]From *Ref.* (Zhang et al., 2018).

Table S6. Surface Component of Cu_1-N_2/HCNS Before and After Reaction[a], related to Figure 4.

Sample	C[b] (At. %)	N[b] (At. %)	O[b] (At. %)	Cu[b] (At. %)	Cu[c] (wt %)
Cu_1-N_2/HCNS	41.84	56.13	1.78	0.25	0.23
Cu_1-N_2/HCNS-*used*	45.72[d]	49.10[d]	4.93[d]	0.25[d]	0.21[e]

[a]Reaction conditions: 20 mg of Cat., 6 mL of CH_3CN, 5.2 mL of H_2O_2, 0.5 mL of benzene, 60 ^oC for 12 h.

[b]XPS results.

[c]ICP-AES results.

[d]The solid catalyst was recovered after 1 cycle.

[e]The solid catalyst was recovered after 4 cycles.

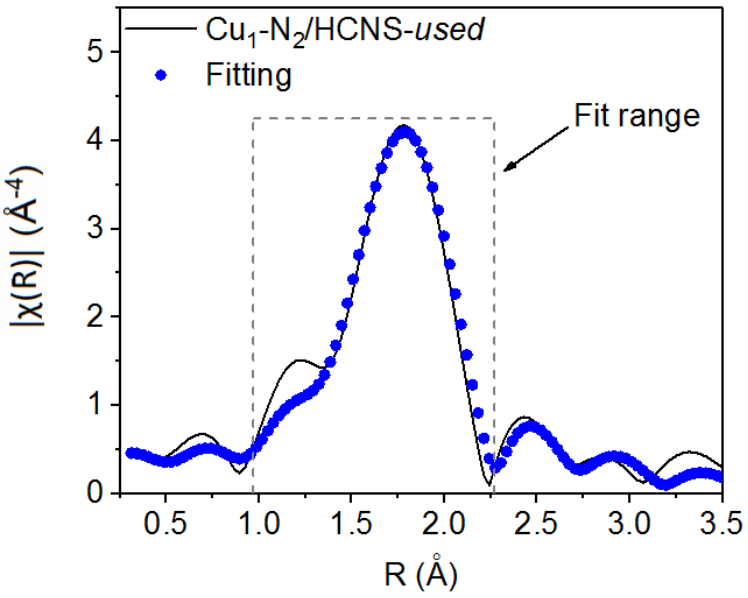

Figure S12. The Corresponding EXAFS Fitting Curve of Cu_1-N_2/HCNS-used Catalyst, related to Figure 4.

Transparent Methods

Chemicals

Melamine, cyanuric acid, copper nitrate hydrate ($Cu(NO_3)_2{\cdot}3H_2O$), acetonitrile (CH_3CN), *n*-tetradecane and chloroform (CH_3Cl) were supplied by Tianjin Fuyu Fine Chemical Co., Ltd. Copper(II) acetate monohydrate ($Cu(OAc)_2{\cdot}H_2O$), dimethyl sulfoxide (DMSO) and H_2O_2 (30%) were purchased from Damao Chemical Reagent Factory. Polyvinylpyrrolidone (PVP-K30) and potassium rhodanate (KSCN) were obtained from Sigma. Nitric acid (HNO_3, 65~68 wt%), sodium hydroxide (NaOH) and sodium borohydride ($NaBH_4$) were supplied by Tianjin Guangfu Technology Development Co., Ltd. All the chemical reagents were analytical grade and directly used without further purification.

Preparation of Hollow Carbon Nitride Spheres (HCNS)

The hollow carbon nitride spheres (HCNS) was prepared corresponding to reference(Jun, 2013; Jun, 2013). Typically, 0.5 g of melamine and 0.51 g of cyanuric acid were ultrosonically dissolved in 20 mL and 10 mL of DMSO, respectively. After that, the two DMSO solutions were mixed together to obtain the white precipitates. As a consequence, the resulting solid was recovered by filtering and washing with ethanol. Finally, the HCNS was obtained by the drying at 50 ^{o}C with the subsequent calcination at 550 ^{o}C for 4 h with the heating rate under nitrogen atmosphere.

Preparation of Cu_1-N_3/HCNS Catalyst

For comparison, the supported Cu_1-N_3 catalyst on HCNS was prepared according to our previous report.(Zhang et al., 2018) Typically, the designed amount of $Cu(NO_3)_2{\cdot}3H_2O$ was firstly mixed with melamine in DMSO and magnetic stirring for 10 min, the DMSO dissolved cyanuric acid was added and keep stirring for 10 min. Solid sample was obtained by filtration and washed with water and ethonal. Dried solid was calcinated under N_2 atmosphere at 550 ^{o}C for 4 h. The finial obtained solid catalyst was denoted as Cu_1-N_3/HCNS. The Cu content is 0.85 wt% determined by ICP-AES.

Preparation of Cu NP/HCNS Catalyst

For comparison, the supported Cu nanoparticle catalyst on HCNS was prepared by a modified adsorption method.(Nishimura, 2010) Typically, a) 0.12 g of PVP-K30 was dissolved in 5 mL of $Cu(OAc)_2{\cdot}H_2O$ aqueous solution (0.02 M) under N_2 atmosphere. b) 1 mL of reductant (1.2 mmol $NaBH_4$ and 1.0 mmol NaOH) was injected and the system was stirring for 12 h. c) 0.5 g of HCNS was added and kept stirring for 4 h. d) Solid sample was recovered by centrifugation and washed with water for 3 times, ethanol for 1 times, respectively. The solid catalyst was dried and denoted as Cu NP/HCNS. The Cu content is 0.85 wt% determined by ICP-AES.

Characterization of Catalysts

Low-magnification field emission scanning electron microscopy (FESEM) images were recorded by a FEI QUANTA 450 scanning electron microscopy. The transmission electron microscopy (TEM), high-resolution TEM, HAADF-STEM images were collected on a JEOL-ARM200F FETEM with 200kV of electron acceleration energy. X-ray photoelectron spectra (XPS) were recorded on an Al Kα radiated Thermo VG ESCALAB250 instrument. The binding energy (BE) was calibrated by C 1s peak at 284.6 eV as the internal standard, and the deconvolution of spectra were carried out using the XPS PEAK 41 program with Gaussian function after subtracted by a Shirley background. Cu content was

determined by an Optima 7300 DV inductively coupled plasma atomic emission spectrometer (ICP-AES). Nitrogen adsorption-desorption isotherms were recorded by 3H-2000PSI system of Beishide apparatus at 77 K. A degas process was performed at 140 ^{o}C for 6 h before the test. Brunauaer-Emmeetr-Teller (BET) model was applied for the analysis of the porosity with the pore volume measured at P/P_0 = 0.99 point. The mesopore size distribution was calculated by BJH method from adsorption branch.

N_2O Titration Experiment

The content of surface active Cu atoms of Cu-NP/HCNS was determined by N_2O titration method on a Builder PCA-1200 apparatus equipped with a thermal conductor detector (TCD).(Zhang et al., 2018; Nishimura, 2010) Typically, a quartz "U" tube loaded with 100 mg sample of Cu-NP/HCNS was equipped and was firstly pretreated with Ar at 300 ^{o}C for 0.5 h. After the sample was reduced by 10 % H_2/Ar at 250 ^{o}C for 0.5 h, the tube was purged with Ar at 35 ^{o}C for 0.5 h. Subsequently, the sample was oxided with N_2O for a period of time. When the TCD baseline stays steady, N_2O was replaced by Ar and the tube was purged for another 0.5 h. Later, the sample was reduced under 10 % H_2/Ar atmosphere at 200 ^{o}C for 0.5 h with a heating rate of 10 ^{o}C/min. The surface consumed H_2 was 3.4 × 10^{-3} mmol calculated through calibration, and the dispersity of Cu active sites was 26 %.

KSCN Titration Experiment

To determine the amount of explosed active Cu on the surface of the single-atom catalysts, KSCN titration method was applied. Typically, 50 mg single-atom catalyst was firstly loaded in a 50 mL flask. Then, a special equivlent of KSCN with 10 mL DI water was added. After magnetic stirring for 2 h, the solid catalyst was separated by centrifugation. Subsequently, the solid catalyst was transferred into the reaction system consist of benzene (0.4 mL), H_2O_2 (6 mL) and acetonitrile (3 mL). The following reaction was performed at 60 ^{o}C for 0.5 h.

XAFS Analysis

The X-ray absorption fine structure (XAFS) spectra at Cu K (E_0= 8979.0 eV) edge was performed at BL14W1 beamline of Shanghai Synchrotron Radiation Facility (SSRF) operated at 3.5 GeV under "top-up" mode with a constant current of 260 mA. The XAFS data were recorded under fluorescence mode with a Lytle-type ion chamber. The energy was calibrated accordingly to the absorption edge of pure Cu foil. Athena and Artemis codes were used to extract the data and fit the profiles. For the X-ray absorption near edge structure (XANES) part, the experimental absorption coefficients as function of energies $\mu(E)$ were processed by background subtraction and normalization procedures, and reported as "normalized absorption" with E_0 = 8979.0 eV for all the tested samples and Cu/Cu_2O/CuO standard. Based on the normalized XANES profiles, the molar fraction of Cu^{2+}/Cu^{+}/Cu^{0} can be determined by the linear combination fit (Kuld, 2014) with the help of various references (Cu foil for Cu^{0}, Cu_2O for Cu^{+} and CuO for Cu^{2+}). For the extended X-ray absorption fine structure (EXAFS) part, the Fourier transformed (FT) data in *R* space were analyzed by applying first-shell appromiate model for Cu-N, Cu-O and Cu-Cu contributions. The passive electron factors, S_0^2, were determined by fitting the experimental data on Cu foil and fixing the coordination number (*CN*) of Cu-Cu to be 12, and then fixed for further analysis of the measured samples. The parameters describing the electronic properties (e.g., correction to the photoelectron energy origin, E_0) and local structure environment including *CN*, bond distance (*R*) and Debye-Waller factor around the absorbing atoms were allowed to

vary during the fit process. The fitted ranges for *k* and *R* spaces were selected to be *k* =3-10 $Å^{-1}$(Cu_1-N_2/HCNS) or 3-12 $Å^{-1}$ (Cu NC/HCNS) with *R* = 1.0–3.0 Å (k^3 weighted).

Computational Methods

The Vienna *ab initio* simulation package (VASP) was applied for all spin-polarized DFT calculations, with the ion cores represented by the projector augmented wave (PAW) potentials(Blöchl, 1994; Kresse, 1996; Kresse, 1999).The generalized gradient approximation (GGA) with the Perdew-Burke-Ernzerhof (PBE) functional(Kresse, 1999) was used to calculate the electronic exchange-correlation energy. A 400 eV of the cutoff energy was used for plane-wavebasis set. Structure optimizations were conducted using a damped molecular dynamics method until the forces on all atoms were less than 0.02 eV/Å. Transition states were searched using the climbing image nudged elastic band (CI-NEB) method(Prdew, 1996; Henkelman, 2000), and each transition state was confirmed to have a single imaginary vibrational frequency along the reaction coordinate.A periodic monolayered *g*-C_3N_4 model ina 2×2 supercell was constructed and the optimized lattice parameters werecalculated to be*a* = *b* = 14.32 Å and *c* = 10.00 Å. A 2×2×1 *k*-point sampling within the Monkhorst-Pack scheme was employed for structural relaxations. The vacuum thickness was set to 10 Å to avoid interactions between repeating slabs. To compare the reactivity of benzene oxidation between the Cu_1-N_2/HCNS and Cu_1-N_3/HCNS catalyst, the C atom at different locations were separately replaced by a single Cu atom to modelthe Cu-N_2 and Cu-N_3 sites, as illustrated in Figure 2i and j. The binding energy of adsorbate was calculated by subtracting the energies of the isolated adsorbate in gas phaseand the bare catalyst from the total energy of the adsorbed system.

Catalytic Performance Test

Selective oxidation of benzene to phenol was performed as the probe evaluation for catalytic performance test. Typically, a certain amount of catalyst (0.046 mg of active Cu atoms, 6 mL of CH_3CN, 0.5 mL of benzene and 5.2 mL of H_2O_2 (30 wt%) were mixed in a 50 mL round-bottom glass flask and sealed carefully. Then the reaction was carried out at 60 ^oC in a water bath kettle with magnetic stirring for a period of time. After the reaction was accomplished and the system cooled down to room temperature, products was extracted by dichloromethane, and *n*-tetradecane was injected as internal standard. The final products was analyzed by Fuli 9790II gas chromatograph equipped with a 30 m × 0.32 mm × 0.50 *μ*m SE-54 capillary column and a flame ionization detector (FID).

Turnover number (*TON*) was calculated as the following formula:

$TON = \Delta n_{Benzene}/n_{Cu}$

$\Delta n_{Benzene}$: Converted benzene, *mol*;

n_{Cu}: Amount of active Cu sites, *mol*.

Kinetic Studies

In order to explain the origin of the extraordinary catalytic performance of the Cu_1-N_2/HCNS catalyst for benzene selective oxidation to phenol, the kinetic studies were performed concerning benzene oxidation and phenol oxidation over diverse catalysts in the temperature range of 20-60 ^oC within a kinetic controlled regime. Reaction conditions: 20 mg of catalyst, 0.20 mL of benzene, 3.0 mL of H_2O_2 (30 wt%), 6 mL of CH_3CN, carried out for 1.5 h at 20 ^oC, 30 ^oC 40 ^oC and 60 ^oC, respectively. The reaction rate (*r*) was calculated by dividing the number of the reacted benzene (phenol) by the

reaction time and the number of the supported active Cu atoms on HCNS. By plotting ln*r* as a function of 1/*T*, an Arrhenius plot was achieved. With the slope and intercept of Arrhenius plot, the apparent activation barrier (E_a) and pre-exponential factor (A) for benzene oxidation and phenol oxidation over the catalysts were achieved.

Recyclability Test

To test the stability of single-atom Cu_1-N_2/HCNS catalyst for benzene selective oxidation to phenol, the recycling experiment was performed. Typically, 20 mg of fresh Cu_1-N_2/HCNS catalyst was applied in a 50 mL round-bottom glass flask. 6 mL CH_3CN, 5.2 mL H_2O_2 and 0.5 mL benzene was added and the flask was sealed carefully. The reaction was carried out at 60 ^oC for 12 h. After one cycle of reaction, solid catalyst was recovered by centrifugation, washed with ethanol and dried. The recovered catalyst was used for the next cycle. Products were analyzed by gas chromatograph.

Controlled experiments

To investigate the origin of the phenol selectivity increment over the recovered single-atom Cu_1-N_2/HCNS catalyst, a rational controlled experiment was performed. Fresh Cu_1-N_2/HCNS catalyst was firstly pretreated with hydrogen peroxide under the same condition as catalytic performance test except benzene was absent. Subsequently, solid catalyst was recovered by centrifugation, washed with ethanol for 3 times and dried. Then, 20 mg of hydrogen peroxide pretreated catalyst was applied in benzene selective oxidation to phenol as the same procedure in recycling test part. The final products were analyzed by gas chromatograph.

Comparative Trials of H_2O_2 Activation over Cu_1-N_2/HCNS and Cu_1-N_3/HCNS

Typically, a certain amount of catalyst (0.046 mg of active Cu atoms, 6 mL of CH_3CN, 1.0 mL of benzene and 0.52 mL of H_2O_2 (30 wt%) were mixed in a 50 mL round-bottom glass flask and sealed carefully. Then the reaction was carried out at 60 ^oC in a water bath kettle with magnetic stirring for a period of time. After the reaction was accomplished and the system cooled down to room temperature, products was extracted by dichloromethane. The remained H_2O_2 was titrated by indirect iodometry method.

The conversion of H_2O_2 was calculated according to the following formula:

$X_{H2O2} = 100\% \times (n^0_{H2O2}-n^1_{H2O2})/n^0_{H2O2}$

X_{H2O2}: H_2O_2 conversion;

n^0_{H2O2}: the initial molar quantity of H_2O_2;

n^1_{H2O2}: the final molar quantity of H_2O_2 after reaction.

The effective utilization rate of of H_2O_2 (U_{H2O2}) was calculated according to the following formula:

U_{H2O2}= 100% x ($\Delta n_{Benzene}$ /Δn_{H2O2})

$\Delta n_{Benzene}$: Converted benzene, *mol*;

Δn_{H2O2}: Converted H_2O_2, *mol*.

Supplemental References

Zhang, T., Zhang, D., Han, X., Dong, T., Guo, X., Song, C., Si, R., Liu, W., Liu, Y. & Zhao, Z. (2018). Preassembly Strategy to Fabricate Porous Hollow Carbonitride Spheres Inlaid with Single Cu−N_3 Sites for Selective Oxidation of Benzene to Phenol. J. Am. Chem. Soc. *140,* 16936-16940.

Zhu, Y., Sun, W., Luo, J., Chen, W., Cao, T., Zheng, L., Dong, J., Zhang, J., Zhang, M., Han, Y., Chen, C., Peng, Q., Wang, D. & Li, Y. (2018). A Cocoon Silk Chemistry Strategy to Ultrathin N-doped Carbon Nanosheet with Metal Single-site Catalysts. Nature Commun. *9,* 3861-3869.

Morimoto, Y., Bunno, S., Fujieda, N., Sugimoto, H. & Itoh, S. (2015). Direct Hydroxylation of Benzene to Phenol Using Hydrogen Peroxide Catalyzed by Nickel Complexes Supported by Pyridylalkylamine Ligands. J. Am. Chem. Soc. *137,* 5867-5870.

Zhang, M., Wang, Y., Chen W., Dong, J., Zheng, L., Luo, J., Wan, J., Tian, S., Cheong, W., Wang, D. & Li, Y. (2017). Metal (Hydr)oxides@Polymer Core-Shell Strategy to Metal Single Atom Materials. J. Am. Chem. Soc. *139,* 10976-10979.

Deng, D., Chen, X., Yu, L., Wu, X., Liu, Q., Liu, Y., Yang, H., Tian, H., Hu, Y., Du, P., Si, R., Wang, J., Cui, X., Li, H., Xiao, J., Xu, T., Deng, J., Yang, F., Duchesne, P. N., Zhang, P., Zhou, J., Sun, L., Li, J., Pan, X., & Bao, X. (2015). A Single Iron Site Confined in a Grapheme Matrix for the Catalytic Oxidation of Benzene at Room Temperature. Sci. Adv. *1,* No. e1500462.

Jun, Y., Park, J., Lee, S. U., Thomas, A., Hong, W. H. and Stucky, G.D. (2013). Three-Dimensional Macroscopic Assemblies of Low-Dimensional Carbon Nitrides for Enhanced Hydrogen Evolution. Angew. Chem. Int. Ed. *52,* 11083-11087.

Jun, Y., Lee, E.Z., Wang, X., Hong, W.H., Stucky, G.D. and Thomas, A. (2013). From Melamine-Cyanuric Acid Supramolecular Aggregates to Carbon Nitride Hollow Spheres. Adv. Funct. Mater. *23,* 3661-3667.

Nishimura, S., Takagaki, A., Maenosono, S. and Ebitani, K. (2010). In Situ Time-Resolved XAFS Study on the Formation Mechanism of Cu Nanoparticles Using Poly(N-vinyl-2-pyrrolidone) as a Capping Agent. Langmuir *26,* 4473-4479.

Kuld, S., Conradsen, C., Moses, P.G., Chorkendorff, I. and Sehested, J. (2014). Quantification of Zinc Atoms in a Surface Alloy on Copper in an Industrial-Type Methanol Synthesis Catalyst. Angew. Chem. *126,* 6051-6055.

Blöchl, P.E. (1994). Projector augmented-wave method. Phys. Rev. B *50,* 17953-17979.

Kresse, G. and Furthmüller, J. (1996). Efficiency of ab-initio total energy calculations for metals and semiconductors using a plane-wave basis set. Comp. Mater. Sci. *6,* 15-50.

Kresse, G. and Joubert, D. (1999). From ultrasoft pseudopotentials to the projector augmented-wave method. Phys. Rev. B *59,* 1758-1775.

Perdew, J.P., Burke, K. and Ernzerhof, M., (1996). Generalized Gradient Approximation Made Simple. Phys. Rev. Lett. *77,* 3865-3868.

Henkelman, G., Uberuaga, B. P. and Jónsson, H., (2000). A climbing image nudged elastic band method for finding saddle points and minimum energy paths. J. Chem. Phys. *113,* 9901-9904.